Materials & Design 237 (2024) 112599

Contents lists available at ScienceDirect

Materials & Design

journal homepage: www.elsevier.com/locate/matdes

Laser polishing and simultaneous hardening of the electrical discharge machined Zr-based metallic glass surface

Jing Hong [a], Hu Huang [a,*], Lin Zhang [b], Zhiyu Zhang [c], Minqiang Jiang [d,e], Jiwang Yan [b]

[a] Key Laboratory of CNC Equipment Reliability, Ministry of Education, School of Mechanical and Aerospace Engineering, Jilin University, Changchun, Jilin, 130022, China
[b] Department of Mechanical Engineering, Faculty of Science and Technology, Keio University, Yokohama 223-8522, Japan
[c] Key Laboratory of Optical System Advanced Manufacturing Technology, Changchun Institute of Optics, Fine Mechanics and Physics, Chinese Academy of Sciences, Changchun, China
[d] State Key Laboratory of Nonlinear Mechanics, Institute of Mechanics, Chinese Academy of Sciences, Beijing 100190, China
[e] School of Engineering Science, University of Chinese Academy of Sciences, Beijing 100049, China

ARTICLE INFO

Keywords:
Laser polishing
Surface hardening
Nanosecond pulsed laser
Metallic glass
Simulation analysis

ABSTRACT

Wire electrical discharge machining (WEDM) is highly suitable for processing the hard-brittle materials like metallic glasses (MGs). However, the electro-thermal energy conversion involved in the WEDM process inevitably introduces some surface defects including bulges, discharge craters, and recast materials on the WEDMed MG surface, which significantly impedes its practical application. Here, an emerging automated polishing technology, laser polishing (LP), was performed in the nitrogen-rich environment to simultaneously improve the surface quality and hardness of the WEDMed Zr-based MG surface. The detailed effects of LP parameters on the surface roughness and morphology were systematically investigated. The morphology evolution and temperature distribution of the molten pool during LP were analyzed by simulation analysis. The experimental results indicated that after single LP of four representative WEDMed Zr-based MG surfaces using the optimized laser parameters, the surface roughness (Sa) was remarkably reduced from 1.27, 2.10, 3.49, and 4.58 μm to 0.09, 0.14, 0.17, and 0.21 μm, respectively, accompanied by an increase in surface hardness from 6.30 GPa to 7.39, 7.67, 8.51 and 8.99 GPa. This study demonstrated that LP could effectively achieve simultaneous enhancement of the quality and hardness of WEDMed MG surfaces, which would contribute to expanding the application prospects of MGs.

1. Introduction

Owing to the inherent structural disorder at the atomic scale, metallic glasses (MGs) possess excellent mechanical properties including high elasticity, strength and hardness, as well as outstanding resistance to wear [1–3]. Nevertheless, a high cooling rate is required to prevent crystallization during high-pressure die casting fabrication of MGs, which makes it difficult to fabricate MGs with large dimension [4]. Thus, MGs currently mainly find the applications in high-end precision products, such as micro-molds, precision surgical instruments, micro-engine parts for mechanical and aerospace applications [5,6]. For the manufacture of these high-end MG components with stringent dimensional accuracy, the mechanical machining techniques such as cutting and milling are commonly employed [7–9]. For instance, Chen et al. [8] explored the relationship between cutting parameters and surface roughness so as to achieve the precision cutting of $Zr_{55}Cu_{30}Al_{10}Ni_5$ MG. Wang et al. [9] employed the cemented carbide cutters to mill microstructures on the MG surface, and then the milled microstructures can serve as tool inserts for the microinjection molding processes, which indicated that the milling process could allow for the precision machining of MGs. Maroju et al. [10] focused on the milling process of MGs, and analyzed the morphology and phase composition of the machined surface. However, the possible oxidation [11,12] and chip formation [13,14] caused by these machining processes, as well as the tool wear when processing the high-hardness materials [15], inevitably impede their application.

Wire electrical discharge machining (WEDM), as a typical non-traditional processing method, involves the melting and vaporization of materials. It is characterized by freedom from material hardness restrictions, low stress-deformation, and less cutting stress. Furthermore,

* Corresponding author.
E-mail address: huanghu@jlu.edu.cn (H. Huang).

https://doi.org/10.1016/j.matdes.2023.112599
Received 4 July 2023; Received in revised form 15 December 2023; Accepted 20 December 2023
Available online 25 December 2023

it is highly suitable for processing the hard-brittle materials and complex structures [16,17]. Hsieh et al. [18] demonstrated the machinability of MG using WEDM, and revealed the relationship between the roughness of the WEDMed surfaces and the WEDM parameters. Chaudhari et al. [19,20] employed WEDM to process a nickel-titanium (Ni55.8Ti) superelastic shape memory alloy, and assessed the impact of optimized process parameters on the material removal rate, surface roughness, and microhardness. Furthermore, they successfully achieved the machining of the nickel-based super-alloy-Udimet 720 (an extremely difficult materials for machining) by means of WEDM [21]. Chen et al. [22] indicated that WEDM can fabricate the hierarchical structures on the surface of 65 vol% SiCp/Al composites, thereby significantly improving its surface hydrophobicity. Despite these advantages, due to the material removal mechanism of WEDM, the specimen surface is typically covered with bulges, discharge craters, and recast materials, consequently diminishing its surface quality [23–25].

To address the defects caused by WEDM, the methods including electrochemical machining, magnetic abrasive finishing, and chemical corrosion could be employed. Among them, electrochemical machining offers the advantages in terms of high-precision processing and small thermal deformation, but it is challenged by the issues like stray current corrosion, complexity of dimensional accuracy control, material waste, and environmental pollution [26,27]. Magnetic abrasive finishing utilizes the magnetic abrasives to scratch the specimen driven by shear force within a magnetic field, thereby enhancing the surface quality [28,29]. Despite this, this method has limitations when processing the small-sized specimens and internal structures such as inner cavities, molds, and narrow grooves. While for chemical corrosion, the protruding portions of the specimen surface could be dissolved in the specific chemical solution [30]. This method usually does not introduce the stress or cracks, and it is suitable for large-area and batch production. But its effectiveness strongly relies on the composition and concentration of the chemical solution used. And the issues such as the edge bluntness, corrosion of sharp features, generation of harmful material waste, and environmental pollution could occur. Therefore, from the aspect of practical application, an appropriate post-processing treatment is urgently pursued for improving the quality of WEDMed MG surface.

Laser polishing (LP), as an emerging automated polishing technique, possesses the characteristics of high precision, rapid processing, non-contact operation, waste-free production, environmental friendliness, and efficient controllability [31–35]. These characteristics of LP allow for its application not only in the surface polishing of multiple materials and the specimens with complex surface morphology (e.g., those machined by WEDM) but also in the precision polishing of the selected area. For instance, Giorgi et al. [32] focused on reducing the surface roughness of AISI 304 stainless steel sheets through employing a fiber laser to induce the material remelting. By effectively repairing cracks and defects, the significant improvements were observed in both surface roughness and surface waviness, with reductions of approximately 58 % and 38 %, respectively. With consideration of the poor surface quality of the laser deposition manufactured components, Xu et al. [33] conducted an investigation on the pulsed LP of TiAl alloy. The results demonstrated a reduction in surface roughness from 16.06 μm (TiAl alloy) to 6.29 μm after pulsed LP. In addition. Sassmannshausen et al. [36] explored the application of ultrashort pulse LP on the tool steel surfaces, which demonstrated the effectiveness of LP for improving the surface quality.

Alongside the investigation of surface quality, the issue of fatigue life of MGs as surface functional materials in practical applications has always received considerable attention. It is widely accepted that surface hardening contributes to enhancing the strength, wear resistance, and impact resistance of load-bearing surfaces, thereby improving their fatigue life. Currently, the studies on surface hardening of MGs primarily focus on the methods such as second-phase strengthening [37,38], phase transformation hardening [39,40], and laser alloying [41,42]. However, the surface quality achieved by these methods is typically unsatisfactory. To the best of our knowledge, there has been limited research focus on addressing the double challenge of significantly improving surface quality and as well effectively enhancing surface hardness. Especially for the difficult-to-machine and defect-ridden rough surfaces, such as those found after WEDM of MGs, there is a notable absence of relevant literature to date. In this study, inspired by the notable improvement of surface hardness of MGs after laser alloying [41,42], the feasibility of LP in a nitrogen-rich environment to simultaneously enhance the surface quality and surface hardness of the WEDMed MG was explored. The as-cast Vit 1 MG ($Zr_{41.2}Ti_{13.8}Cu_{12.5}Ni_{10}Be_{22.5}$) was chosen as the test material because of its high glass forming ability and commercial availability. The detailed effects of LP parameters including the pulse width, pulse frequency, laser power, scanning speed, and number of LP on surface roughness and morphology were systematically investigated. The temperature distribution and morphology evolution of molten pool during LP were analyzed by simulation analysis. Furthermore, nano-indentation tests were employed to evaluate the hardness of the LP surface.

Table 1
Chemical composition of the Zr-based MG.

Element	Zr	Ti	Cu	Ni	Be
Composition (at. %)	41.2	13.8	12.5	10	22.5

2. Experimental details

2.1. WEDM process of Zr-based MG

The as-cast Vit 1 MG ($Zr_{41.2}Ti_{13.8}Cu_{12.5}Ni_{10}Be_{22.5}$) (Peshing New Metal Material (Changzhou) Co., Ltd., China) was employed as the specimen, given that it is now conveniently acquired and possesses compositional homogeneity as a result of multiple re-melting during the copper mold suck-casting [43,44], and the detailed chemical composition is listed in Table 1. It is worth noting that Vit 1 MG contains Be, which is a relatively small metallic atom. This atom holds promise for occupying the voids within the defective regions of MGs, thereby effectively stabilizing the liquid and glass phases. Furthermore, Vit 1 MG exhibits the high glass forming ability, which paves the way for the large-scale production of MGs using the traditional casting process and opens up new avenues for their expanded applications across various fields [45,46]. Then, for preparing the WEDMed Zr-based MG surface, a reciprocating type wire cut electrical discharge machining (DK7750, nantong womu mechanical and electrical equipment engineering Co., Ltd., China) was utilized. A molybdenum wire with a diameter of 0.18 mm was employed in the WEDM process. Subsequently, under a stable feeding path, a strip-shaped specimen of Zr-based MG (dimension: 20 mm × 2 mm × 2 mm) with a WEDMed surface was fabricated as illustrated in Fig. 1. Fundamentally, the WEDM process is characterized by the conversion of the electro-discharge energy into thermal energy between the tool electrode and the specimen, and its electro-discharge energy depends on the WEDM process parameters including pulse spacing, discharge current and pulse duration [47]. Thus, the WEDMed surface quality strongly depends on the WEDM process parameters. In order to verify the feasibility of LP, four WEDMed MG surfaces with varied surface roughness were prepared by adjusting the WEDM process parameters. For clarity, different sets of the WEDM process parameters in Table 2 are referred to as WEDM 1, WEDM 2, WEDM 3, and WEDM 4.

2.2. LP of the WEDMed Zr-based MG

Thereafter, LP of the WEDMed MG surfaces was performed by using a fiber nanosecond pulsed laser (SP-050P-A-EP-Z-F-Y, SPI Lasers, UK). Fig. 2(a) displays the detail schematic of LP process. Specifically, a high-frequency pulsed laser beam passes through a pair of mirrors and a F-theta lens in the optical path system, and then is directed to the WEDMed MG surface for final focusing. To protect the specimen from

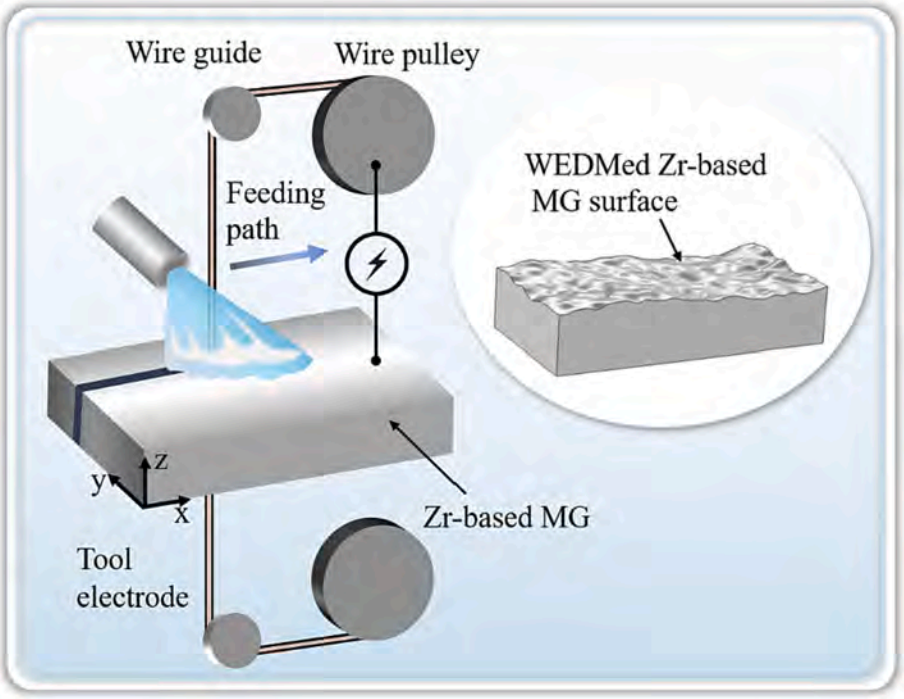

Fig. 1. Schematic illustrating the WEDM process.

Table 2
WEDM process parameters of the Zr-based MG.

	Pulse spacing (μs)	Pulse duration (μs)	Discharge current (A)
WEDM 1	10	2	30
WEDM 2	8	8	40
WEDM 3	4	30	40
WEDM 4	4	40	50

oxidation while enhancing the surface hardness of MG, a nitrogen atmosphere was employed during the LP process. The scanning strategy adopted for LP is zig-zag pattern as displayed in Fig. 2(b), where the laser beam moves by 2 mm, then offsets by 8.9 μm in relation to the preceding scanning path and before performing another line irradiation.

The continuous laser irradiation of WEDMed MG surface results in the formation of a molten pool. Within this molten pool, the liquid materials would experience redistribution (Fig. 2(c)), which results in a reduction of surface roughness [48,49]. For investigating the surface roughness under different LP parameters, systematic experiments were performed

Table 3
Laser parameters for polishing the WEDMed surfaces.

LP parameter	Nomenclature	Value
Laser power (W)	P	7.12, 8.82, 10.5, 12.1, 13.7
Scanning speed (mm/s)	V	200, 300, 400, 500, 600
Pulse frequency (kHz)	f_r	400, 600, 800, 1000
Pulse width (ns)	p_t	10, 20, 30

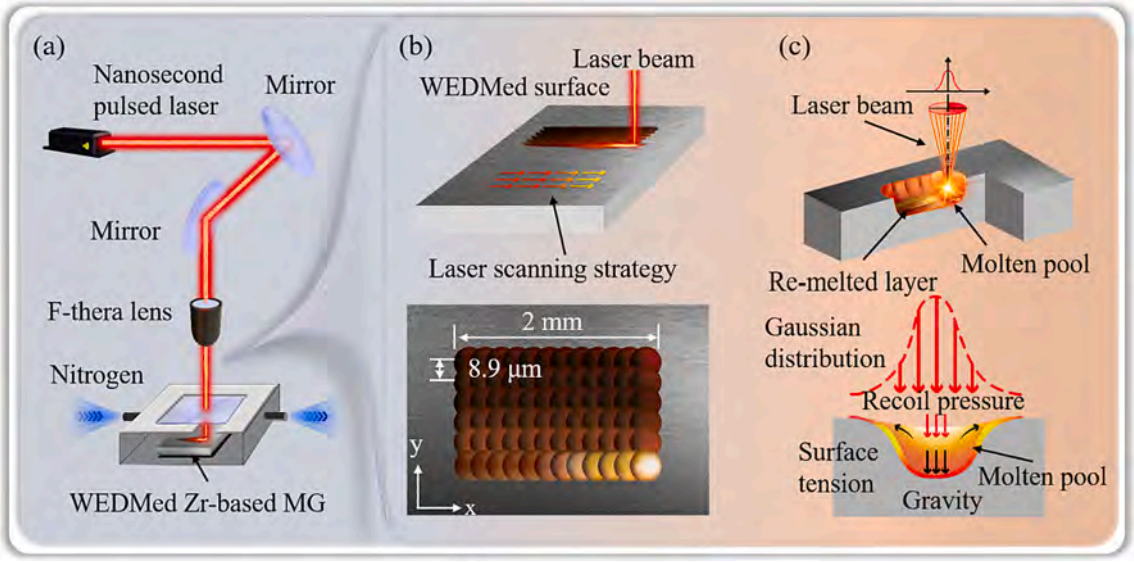

Fig. 2. Schematic view showing (a) LP experimental setup, (b) adopted LP scanning strategy, and (c) LP principle.

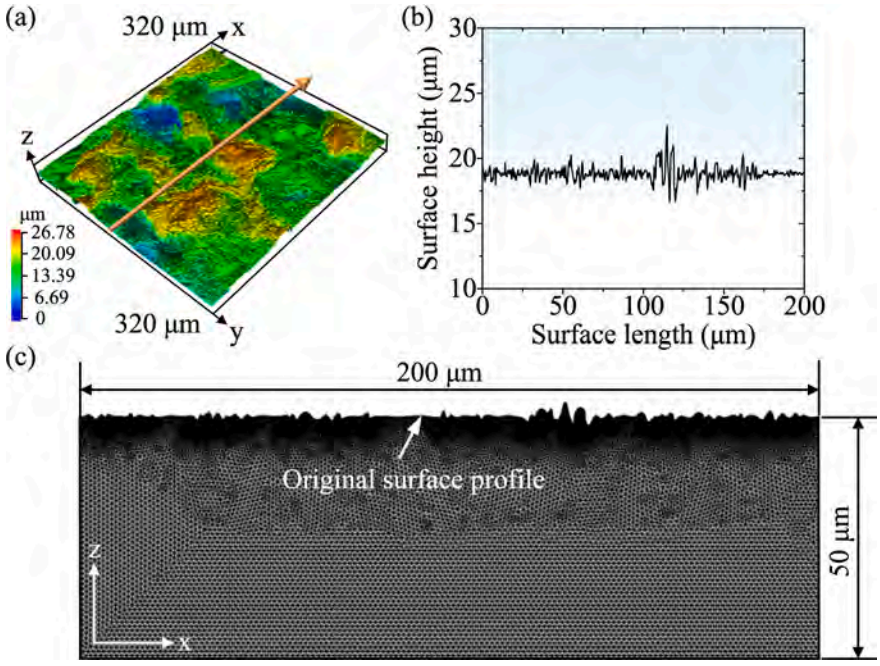

Fig. 3. (a) Three-dimensional (3D) contour of the WEDMed surface; (b) 2D surface profile derived from 3D contour in Fig. 3(a); (c) 2D simulation model.

using the laser parameters listed in Table 3.

2.3. Simulation analysis of LP process

To further clarify the complex hydrodynamics behavior that occurs during LP process and reveal the underlying mechanism of surface morphology evolution, the simulation analysis was carried out through COMSOL Multiphysics finite element software. A two-dimensional (2D) model was developed, where the 2D experimental profile data of the WEDMed Zr-based MG was firstly imported into the 2D transient model to initialize the surface profile (Fig. 3(a) and (b)). Then, with consideration of the occurrence of singularities owing to the high-frequency noise of the optical profile during geometric modeling, the imported 2D profile data were parameterized. Accordingly, the 2D model with a dimension of 200 μm × 50 μm was established in Fig. 3(c). During simulation, a pulsed laser with Gaussian distribution, serving as a heat source, is directed onto the WEDMed surface and moves along the *x* axis. Accordingly, the surface materials begin to melt, generating a molten pool. To identify the transient temperature and velocity, the heat transfer and laminar flow modules are employed, and these modules rely on solving energy conservation equation (see Eq. (1)) and momentum conservation equation (see Eq. (6))[67], respectively.

$$\rho C_P\left[\frac{\partial H(x,t)}{\partial t}+\nabla\left(\overrightarrow{\mathscr{F}}H(x,t)\right)\right]-\nabla(k\nabla H(x,t))=\mathscr{I}(x,t)+Q_{evap}(H(x,t)) \tag{1}$$

where ρ, C_p, and k mean the density, specific heat capacity, and thermal conductivity of the Zr-based MG. $H(x,t)$ and $\overrightarrow{\mathscr{F}}$ present the temperature and flow velocity. $\mathscr{I}(x,t)$ is the peak laser power intensity. $Q_{evap}(H(x,t))$ stands for the energy loss caused by the surface evaporation, which is expressed by Eqs. (3)–(5),

$$\mathscr{I}(x,t)=\frac{2\varepsilon P}{\pi f_r p_t \omega_0^2}\exp\left(-2\frac{(x-x_0+Vt)^2}{\omega_0^2}\right) \tag{2}$$

$$Q_{evap}(H(x,t))=M_v(H(x,t))L_v \tag{3}$$

$$M_v(H(x,t))=\frac{(1-\beta_r)}{\sqrt{2\pi k_{\mathbb{B}}}}\sqrt{\frac{M}{H(x,t)}}P_{sat}(H(x,t)) \tag{4}$$

$$P_{sat}(H(x,t))=P_0\exp\left(\frac{L_v M}{\overline{H_v}k_{\mathbb{B}}}\left(1-\frac{\overline{H_v}}{H(x,t)}\right)\right) \tag{5}$$

where P, f_r, p_t, ω_0, ε, x_0, and V are the laser power, pulse frequency, pulse width, spot radius, absorption coefficient, initial position, and scanning speed of laser beam. $M_v(H(x,t))$ stands for the mass of particles escaping from the molten pool; β_r, $k_{\mathbb{B}}$, P_0, $P_{sat}(H(x,t))$ are the inverse diffusion coefficient, Boltzmann constant, atmospheric pressure, and saturated vapor pressure; L_v, $\overline{H_v}$, and M represent the latent heat of evaporation, evaporation temperature, and molar mass of the Zr-based MG.

The momentum conservation equation is expressed as

$$\rho\left[\frac{\partial\rightarrow\mathscr{F}}{\partial t}+\rightarrow\mathscr{F}\left(\nabla\rightarrow\mathscr{F}\right)\right]=\nabla\left[-P_{total}\boldsymbol{I}+\mu\left(\nabla\rightarrow\mathscr{F}+\left(\nabla\rightarrow\mathscr{F}\right)^T\right)\right]+\rho g+\rightarrow f_{mush}+\rightarrow G \tag{6}$$

$$\overrightarrow{f_{mush}}=-A_{mush}\frac{(1-\mathscr{B}^2)}{\mathscr{B}^3+C}\overrightarrow{\mathscr{F}} \tag{7}$$

$$\mathscr{B}=flc2hs((H-\overline{H_m}),(\overline{H_l}-\overline{H_s})) \tag{8}$$

$$\overrightarrow{G}=-P_{sat}(H(x,t))\overrightarrow{n}+\gamma(\nabla_t\overrightarrow{n})\overrightarrow{n}-\frac{\partial\gamma}{\partial H(x,t)}\nabla_t H(x,t)\overrightarrow{t} \tag{9}$$

where $\overline{H_m}$, $\overline{H_l}$, $\overline{H_s}$, μ, and γ stand for the melting temperature, liquidus temperature, solidus temperature, viscosity, and surface tension of the Zr-based MG. $\boldsymbol{I}$, g, and P_{total} stand for the identity matrix, gravity constant as well as the total pressure of molten pool. $\overrightarrow{f_{mush}}$ is Darcy damping force which expresses the energy dissipation of the mushy region. A_{mush}, C, and $\mathscr{B}$ stand for the permeability coefficient that can control the shape of the mushy region, a quite small constant, and liquid volume fraction. $\overrightarrow{G}$ means the body force in the molten pool. Additionally, the

Table 4
Thermal physical parameters of the Zr-based MG.

Thermal physical parameter	Nomenclature	value
Density of solid (g/cm^3)	ρ_s	6.125 [50]
Density of liquid (g/cm^3)	ρ_l	6.02 [51]
Thermal conductivity of solid (W/(m × K))	k_s	16 [52]
Thermal conductivity of liquid (W/(m × K))	k_l	17 [52]
Specific heat capacity of solid (J/(kg × K))	C_{ps}	674 [52]
Specific heat capacity of liquid (J/(kg × K))	C_{pl}	684 [52]
Latent heat of melting (J/mol)	L_m	6184 [46]
Latent heat of evaporation (J/mol)	L_v	438,000 [53]
Solidus temperature (K)	$\overline{H_s}$	937 [46]
Liquidus temperature (K)	$\overline{H_l}$	993 [46]
Melting temperature (K)	$\overline{H_m}$	965 [53]
Evaporation temperature (K)	$\overline{H_v}$	3792 [53]
Molar mass (g/mol)	M	60.3 [52]

detailed thermal physical parameters of the Zr-based MG are listed in Table 4.

2.4. Characterization

The microstructural characteristics of the WEDMed MG surfaces before and after LP were investigated by the tungsten filament scanning electron microscope (SEM, JSM-IT500A, JEOL, Japan). The 3D contours and surface roughness values were analyzed by using the laser scanning confocal microscope (LSCM, OLS4100, Olympus, Japan). The hardness of the LP surfaces was evaluated using a nanoindentation instrument (DUH-211, SHIMADZU, Japan). A specific indentation load of 120 mN and a loading rate of 10 mN/s were employed. To more clearly demonstrate the variation of surface hardness, the morphologies of the residual indentations were captured by SEM. And the phase constituent changes experienced from the WEDMed MG surface during LP were examined by an X-ray diffractometer (XRD, D8 Discover, Bruker, Germany). An energy dispersive X-ray spectroscopy (EDS, EX-74600U4L2Q, JEOL, Japan) was used to investigate the element distribution along the depth direction of the WEDMed MG surface and LP region.

3. Results

3.1. Removal effect of LP

Fig. 4 illustrates the comparison of the SEM morphologies between the WEDMed MG surfaces obtained under the parameters in Table 2 (named as WEDMS1, WEDMS2, WEDMS3, and WEDMS4) and the corresponding single LP surfaces (named as SLP1, SLP2, SLP3, and SLP4). The WEDMS1-WEDMS4 surfaces exhibit quite rough texture, characterized by plenty of discharge craters and recast materials as depicted in Fig. 4(a), (b), (d), (e), (g), (h), (j), and (k). These surface features are associated with the electro-thermal process during WEDM [25,54]. Specifically, when the Zr-based MG block is subjected to high electro-discharge energy, the interface materials between MG and the tool electrode undergo melting and potentially even evaporation, thus leading to the rough WEDMed surfaces. However, after performing single LP with the optimized parameters as listed in Table 5, the initial surface features for all investigated cases have completely disappeared, and the smoother surfaces compared to the WEDMed surfaces are generated as presented in Fig. 4(c), (f), (i), and (l). Meanwhile, some laser-remelted tracks along the laser scanning direction as well as slight spatial undulation features can be visible, and the existing subtle bumps and pits on the SLP1-SLP4 surfaces are marked by dotted lines. Then, the areal surface roughness (Sa) as a metric is employed to quantitatively evaluate the surface quality, and the results are illustrated in Fig. 5, where the roughness of the WEDMS1-WEDMS4 surfaces is remarkably reduced from 1.27, 2.10, 3.49, and 4.58 μm to 0.09, 0.14, 0.17, and 0.21 μm, respectively, after single LP. In summary, the evolution of the surface microstructure and surface roughness indicate an evident improvement of the surface flatness by using LP, regardless of whether the test specimen is WEDMS1, WEDMS2, WEDMS3 or WEDMS4.

On the other hand, it is noted that among the optimized single LP parameters in Table 5, the pulse width exhibits a more pronounced difference in comparison with the other parameters, i.e., the pulse width is 10 ns for WEDMS1 and WEDMS2 surfaces, while for WEDMS3 and WEDMS4 surfaces, it is 20 ns and 30 ns, respectively. This is because, as the WEDM process proceeds from WEDM1 to WEDM4 (see Table 2), the increase of pulse duration and discharge current would cause more discharge energy to be released and penetrate into the materials, thereby leading to an increase in the dimension of the discharge craters and apparent surface undulations [47]. Given that the pulse width during LP determines the energy emission time of laser beam [55], thus, to provide sufficient time for the molten micro-peak materials to flow into the micro-valleys so that the initial morphologies of the WEDMed surfaces are sufficiently melted, the pulse widths of WEDMS3 and WEDMS4 surfaces are determined to be increased.

3.2. Hardness of LP surface

To evaluate the mechanical properties of the SLP1-SLP4 surfaces at the micro-scale, nanoindentation tests were conducted. Fig. 6(a) and (b) present the surface hardness and the corresponding load-depth curves. Obviously, a maximum hardness (8.99 GPa) is obtained for SLP4, followed by SLP3 (8.51 GPa), and the surface hardness for SLP1 and SLP2 is 7.39 GPa and 7.67 GPa, respectively. These statistical results can be supported again by the SEM morphologies of the residual indentations presented in Fig. 6(c)–(g), from which a gradual decreasing trend in the dimension of these indentations from the as-cast MG to SLP4 is observed. From the aforementioned results, it is evident that the SLP1-SLP4 surfaces exhibit a higher hardness than the as-cast MG surface, suggesting an enhancement in the mechanical properties of the as-cast MG surface after WEDM and subsequent LP.

To clarify the reason for the above phenomenon, the crystalline phases of the WEDMS1-WEDMS4 surfaces, SLP1-SLP4 surfaces, and as-cast MG are examined by XRD. It is visible that the XRD spectrum of as-cast MG specimen exhibits a typical broad diffuse peak at about 38° in Fig. 7(a), indicating its amorphous feature. In contrast, the XRD spectrum of the WEDMS1-WEDMS4 surfaces exhibits several crystalline peaks with small intensities that are embedded in the XRD spectrum of as-cast MG (Fig. 7(a)). By retrieving phase with JADE software, these crystalline peaks are determined as the ZrO_2 phase, which may arise from the oxidation that occurs during WEDM. While for the SLP1-SLP4 surfaces, except for preserving the diffraction peaks occurring in the spectrum of the WEDMed surfaces, some new peaks with greater intensities are detected at the diffraction angles of 34.42°, 39.82°, 57.54°, 68.78°, and 72.24°, which can be identified as the ZrN phase (Fig. 7(b)). The generation of ZrN phase can be ascribed to the utilization of the nitrogen-rich environment during the LP process, which facilitates the introduction of the ZrN phase to the MG substrate [41,42]. Since ZrN phase possesses intrinsically high hardness, so it is potentially responsible for the increased surface hardness. Additionally, the in-situ formed ZrN phase acts as the secondary phase in MG substrate, which could involve the large amount of crystal defects and stimulate the formation of multiple shear bands. Accordingly, the resistance to plastic deformation is enhanced, contributing to its surface hardening [56].

Additionally, ZrN content exhibits a rising tendency from SLP1 to SLP4, which is supported by the intensified ZrN diffraction peaks in Fig. 7(b). By analyzing the LP parameters in Table 5, it is evident that the pulse width is the main factor affecting the ZrN content. The physical mechanism behind it may be that the increase of the pulse width can allow for an extended residence time of laser irradiation, promoting the reaction between the MG material and the surrounding nitrogen [57]. Furthermore, it should be mentioned that the SLP1 surface possesses the same pulse width as the SLP2 surface, but the intensity of ZrN phase in

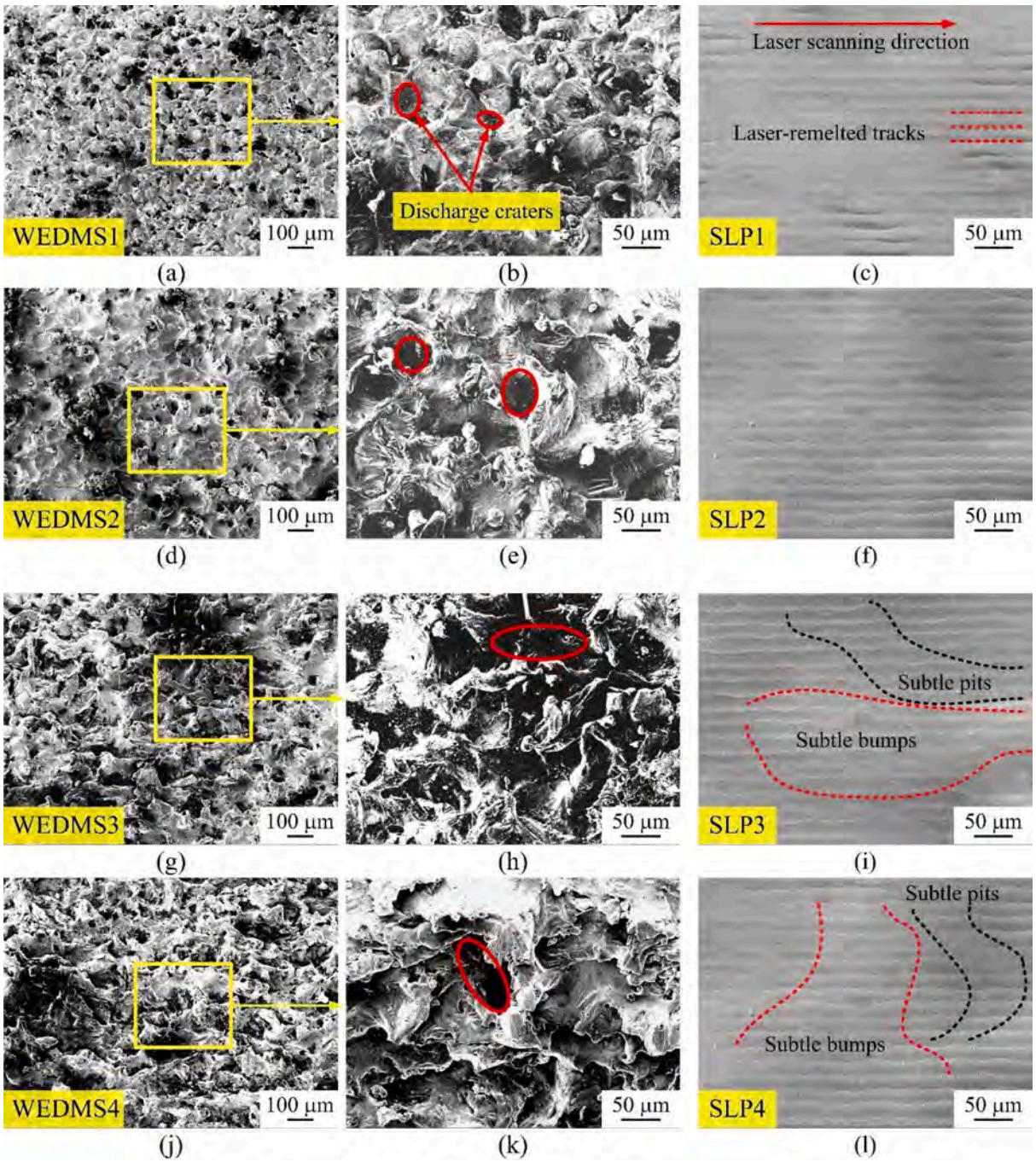

Fig. 4. SEM morphologies of the WEDMed MG surfaces: (a)–(b) WEDMS1, (d)–(e) WEDMS2, (g)–(h) WEDMS3, (j)–(k) WEDMS4 as well as the corresponding LP surfaces: (c) SLP1, (f) SLP2, (i) SLP3, (l) SLP4.

Table 5
Optimized single LP parameters for each WEDMed surface.

	Laser power (W)	Scanning speed (mm/s)	Pulse frequency (kHz)	Pulse width (ns)
WEDMS1	10.5	400	800	10
WEDMS2	10.5	400	1000	10
WEDMS3	10.5	400	1000	20
WEDMS4	10.5	400	1000	30

the diffraction spectrum of the SLP2 surface is slightly higher compared to the SLP1 surface. This phenomenon could be correlated with the surface roughness, i.e., the roughness of WEDMS2 surface is slightly larger than that of WEDMS1 surface, which means that more laser energy would be absorbed for WEDMS2 surface [58]. According to the above analysis, it can be concluded that in comparison with as-cast MG surface, the hardness of the SLP1-SLP4 surfaces exhibits a pronounced increase. This improvement in hardness can be primarily ascribed to the formation of ZrN phase.

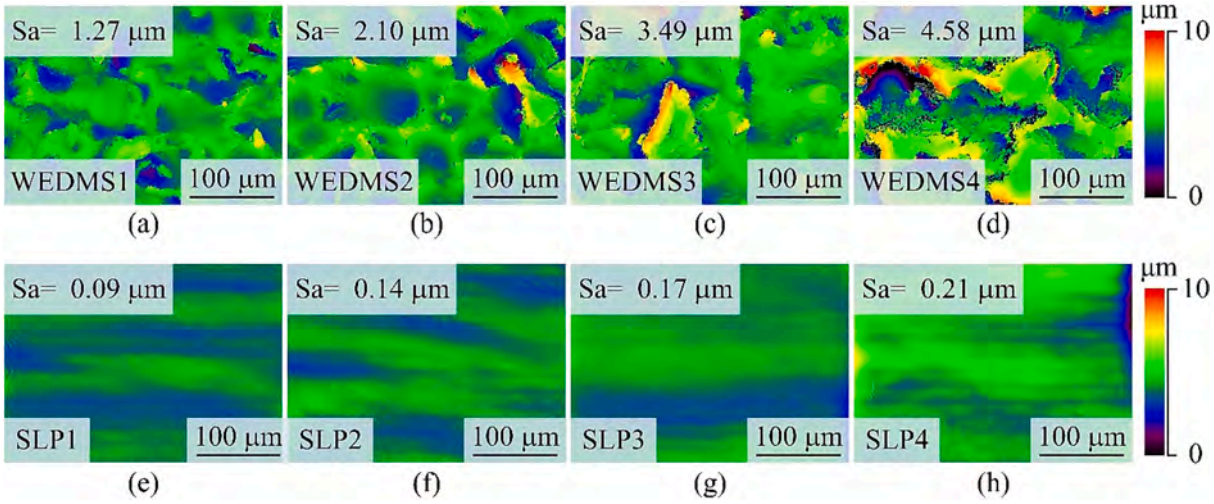

Fig. 5. 3D surface contours of (a)–(d) WEDMed MG surfaces and (e)–(h) SLP1-SLP4 surfaces.

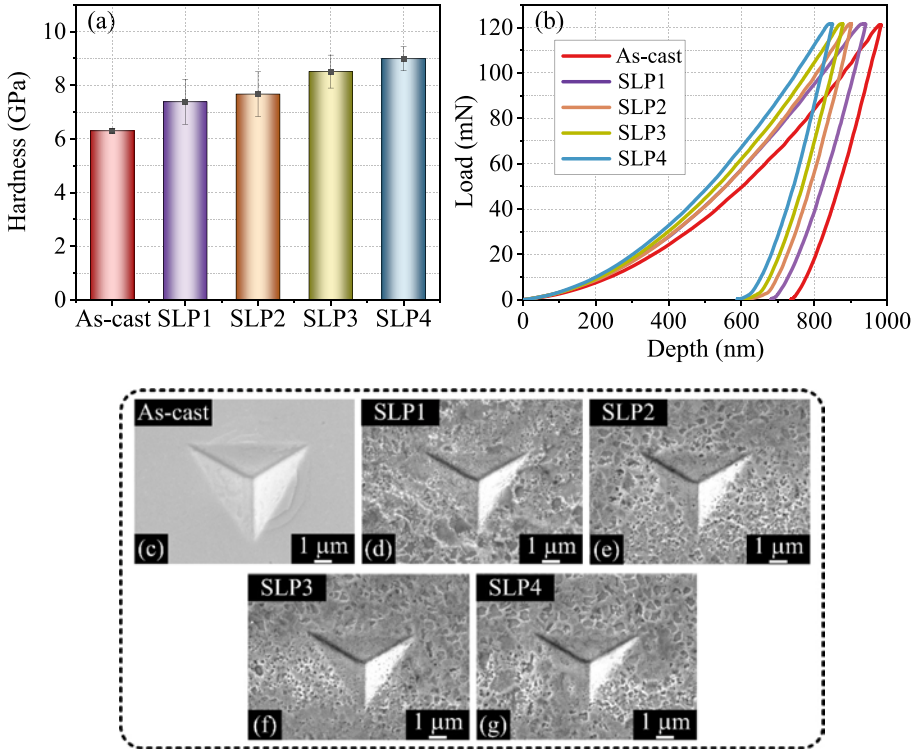

Fig. 6. (a) Surface hardness and (b) load-depth curves of as-cast MG as well as the SLP1-SLP4 surfaces. Fig. 6(c)–(g) show the residual indentations on the as-cast MG as well as SLP1-SLP4 surfaces, respectively.

4. Discussion

4.1. Surface roughness evolution

To achieve a more thorough comprehension of LP, a quantitative analysis is performed on the variation of roughness of the WEDMS1-WEDMS4 surfaces with the laser power (7.12 W–13.7 W), scanning speed (200 mm/s–600 mm/s), and pulse frequency (400 kHz–1000 kHz). The obtained results from Fig. 8 clearly demonstrate that the roughness of the WEDMS1-WEDMS4 surfaces is highly sensitive to LP parameters, and Sa and Sz exhibit similar variation trends when subjected to the same LP parameter.

For sake of brevity, a detailed analysis of surface roughness variation with different LP parameters is presented specifically for WEDMS4 surface. As illustrated in Fig. 8(j), an increase in laser power (7.12–10.5 W) leads to a gradual decrease in surface roughness (Sa) (0.375–0.243 μm), resulting in a minimal surface roughness. However, with a further increase in laser power (10.5–13.7 W), an opposite trend is observed for the surface roughness (Sa), increasing from 0.243 μm to 0.322 μm. This implies that the surface smoothing behavior is weakened when using a relatively large laser power. Subsequently, the surface roughness variation with scanning speed from 200 mm/s to 600 mm/s is investigated by keeping a fixed laser power of 10.5 W. As is depicted in Fig. 8(k), surface roughness initially decreases (200–400 mm/s) and subsequently increases (400–600 mm/s). After setting the laser power (10.5 W) and scanning speed (400 mm/s), the surface roughness changing with pulse

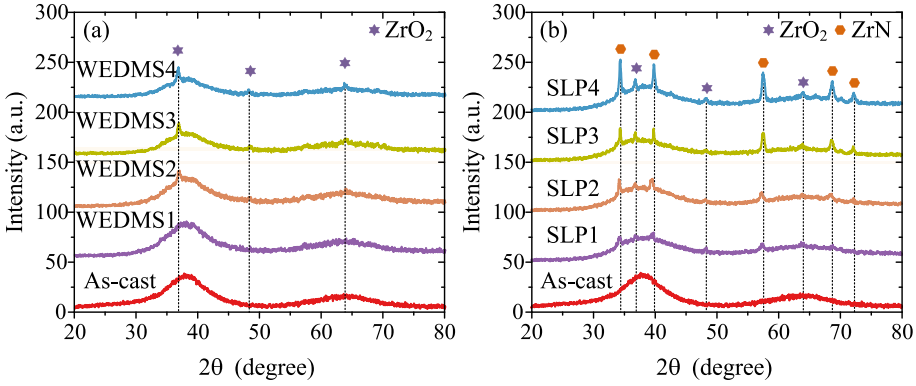

Fig. 7. XRD spectrums of (a) the WEDMS1-WEDMS4 surfaces and (b) the SLP1-SLP4 surfaces.

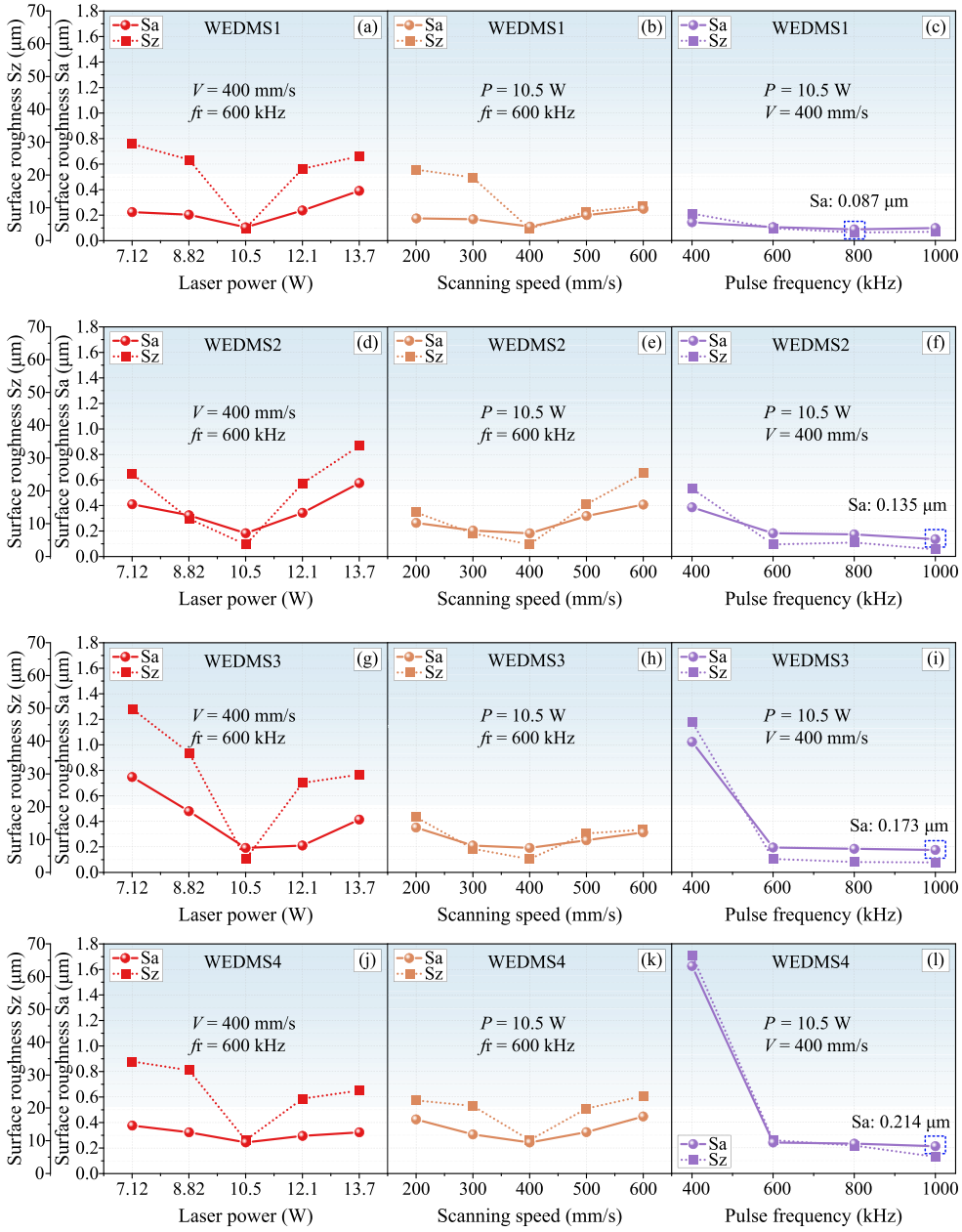

Fig. 8. Surface roughness (Sa and Sz) changing with LP parameters for (a)–(c) WEDMS1, (d)–(f) WEDMS2, (g)–(i) WEDMS3, and (j)–(l) WEDMS4.

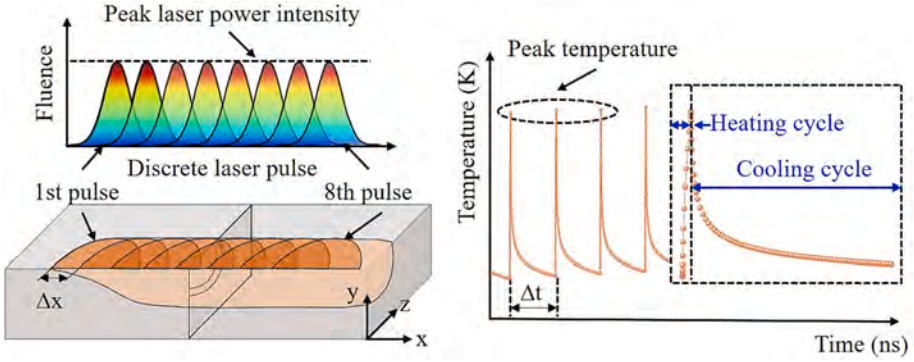

Fig. 9. Schematic illustrating the spatial distance and time interval between the adjacent laser pulses.

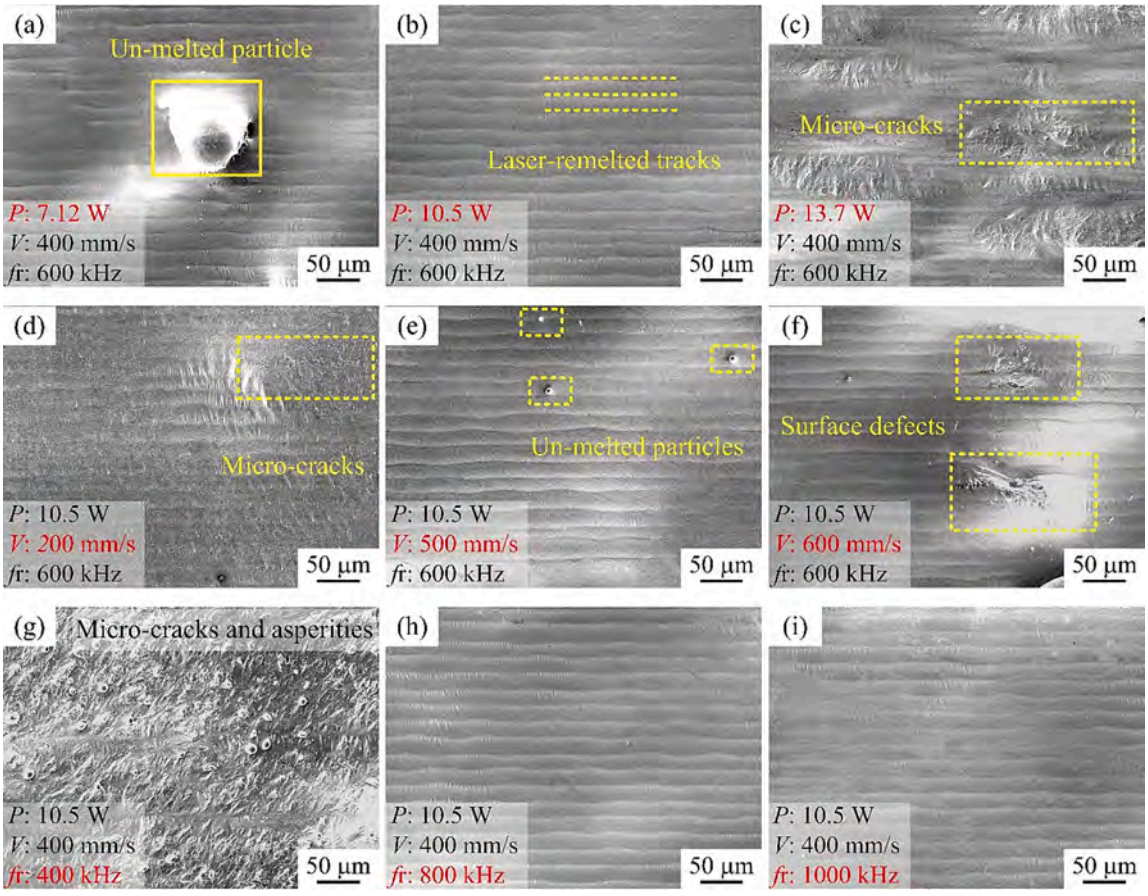

Fig. 10. Effect of (a)–(c) laser power, (d)–(f) scanning speed, and (g)–(i) pulse frequency on morphology of WEDMS4 surface.

frequency is further explored in Fig. 8(l), where the surface roughness (Sa) drops from 1.626 μm to 0.243 μm with the pulse frequency increasing from 400 kHz to 600 kHz, after which it slowly continues to decrease until the pulse frequency increases to 1000 kHz.

From above analyses, it is evident that selecting appropriate LP parameters plays a critical role in achieving effective reduction of surface roughness. Fundamentally, pulsed LP is a complex thermodynamic process characterized by the emission of a series of discrete laser pulses with Gaussian distribution [35,59]. Irradiated by the pulsed laser, a transient high-temperature region is generated, and the resulting temperature change over time can be described by a series of thermal cycle profiles as presented in Fig. 9. Every thermal cycle profile can be divided into two distinct stages: the heating cycle and the cooling cycle. During the heating cycle, LP region absorb the irradiation energy from the pulsed laser, resulting in the increased surface temperature. Thereafter, the LP region undergoes a phase change from solid to liquid, forming a molten pool [60,61]. This allows for the liquid materials in the molten pool to flow from micro-peaks to micro-valleys. As the laser is turned off, LP region experiences a gradual decrease in temperature, initiating the cooling cycle. In this process, the detailed melting state of molten pool and its temperature distribution are controlled by the LP parameters including the pulse width, laser power as well as pulse frequency, since they could affect the heat input (i.e., peak laser power intensity) (Eq. (10)) [62],

$$\mathscr{I}_p = \frac{P}{f_r p_t \pi \omega_0^2} \tag{10}$$

Furthermore, the distribution of the discrete laser pulses also affects

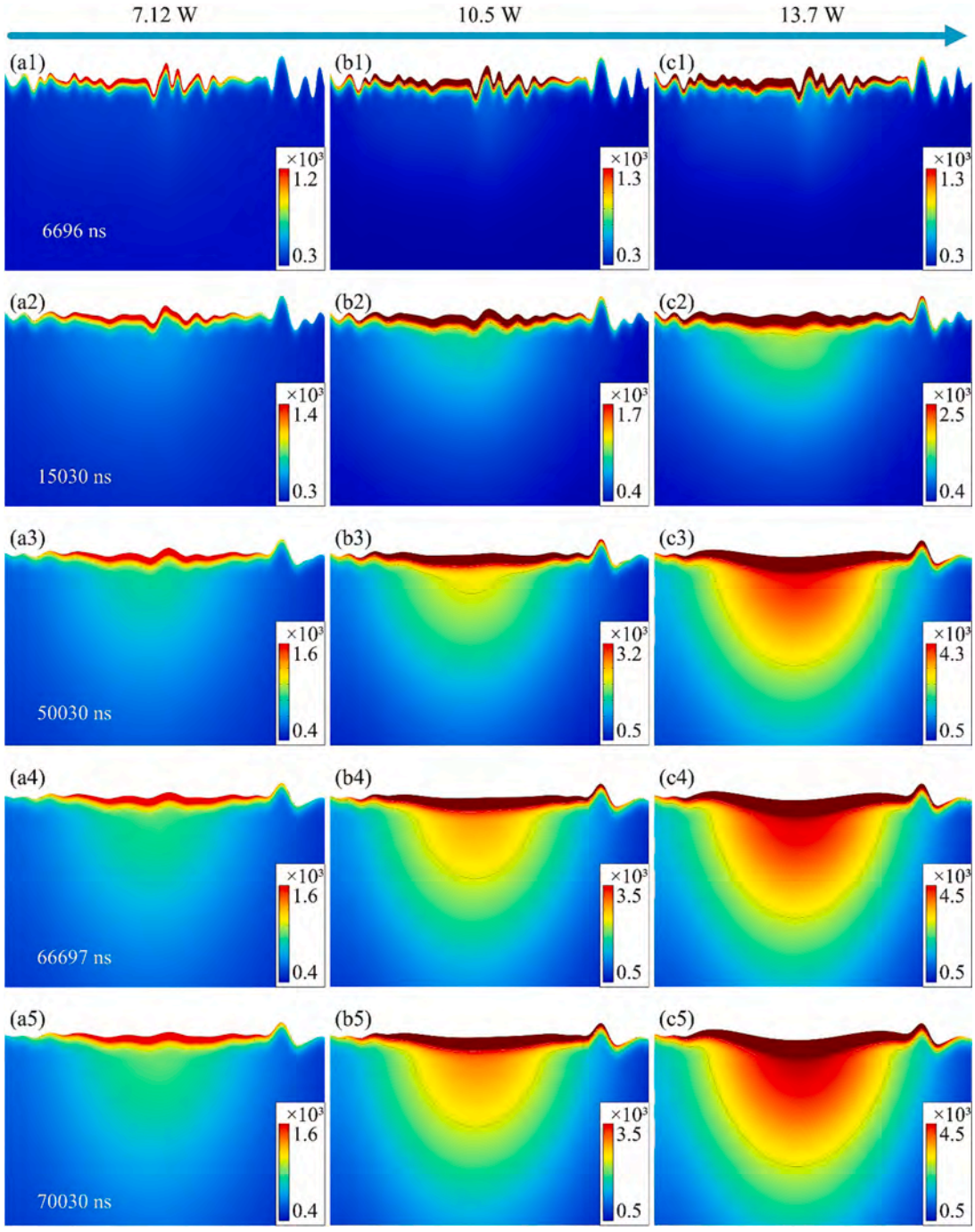

Fig. 11. Instantaneous change in the contours of molten pools at the laser power of (a1)-(a5) 7.12 W, (b1)-(b5) 10.5 W, (c1)-(c5) 13.7 W.

the redistribution of the liquid materials. Referring to the following equations [55],

$$\Delta x = \frac{V}{f_r} \tag{11}$$

$$\Delta t = \frac{1}{f_r} \tag{12}$$

It is evident that the spatial distance Δx and the time interval Δt between the adjacent laser pulses depend on scanning speed and pulse frequency (see Fig. 9). Accordingly, these two laser parameters determine the surface remelting times per unit area or per unit time, thereby exerting a pivotal influence on the extent of heat accumulation. In summary, the above laser parameters jointly influence the temperature distribution and flow behavior of molten pool, and determine the final effect of LP.

4.2. Surface morphology evolution

To gain a more profound insight into the LP, the morphology evolution of the WEDMS4 surface under different LP parameters is investigated, and the SEM morphologies of some representative LP surfaces are illustrated in Fig. 10. As displayed in Fig. 10(a)–(c), the initial contours caused by the WEDM process have been eliminated under these three LP conditions. Simultaneously, some distinctive morphological features emerge from the LP surfaces. Specifically, the evident undulations and residual particles appear on the SEM morphology

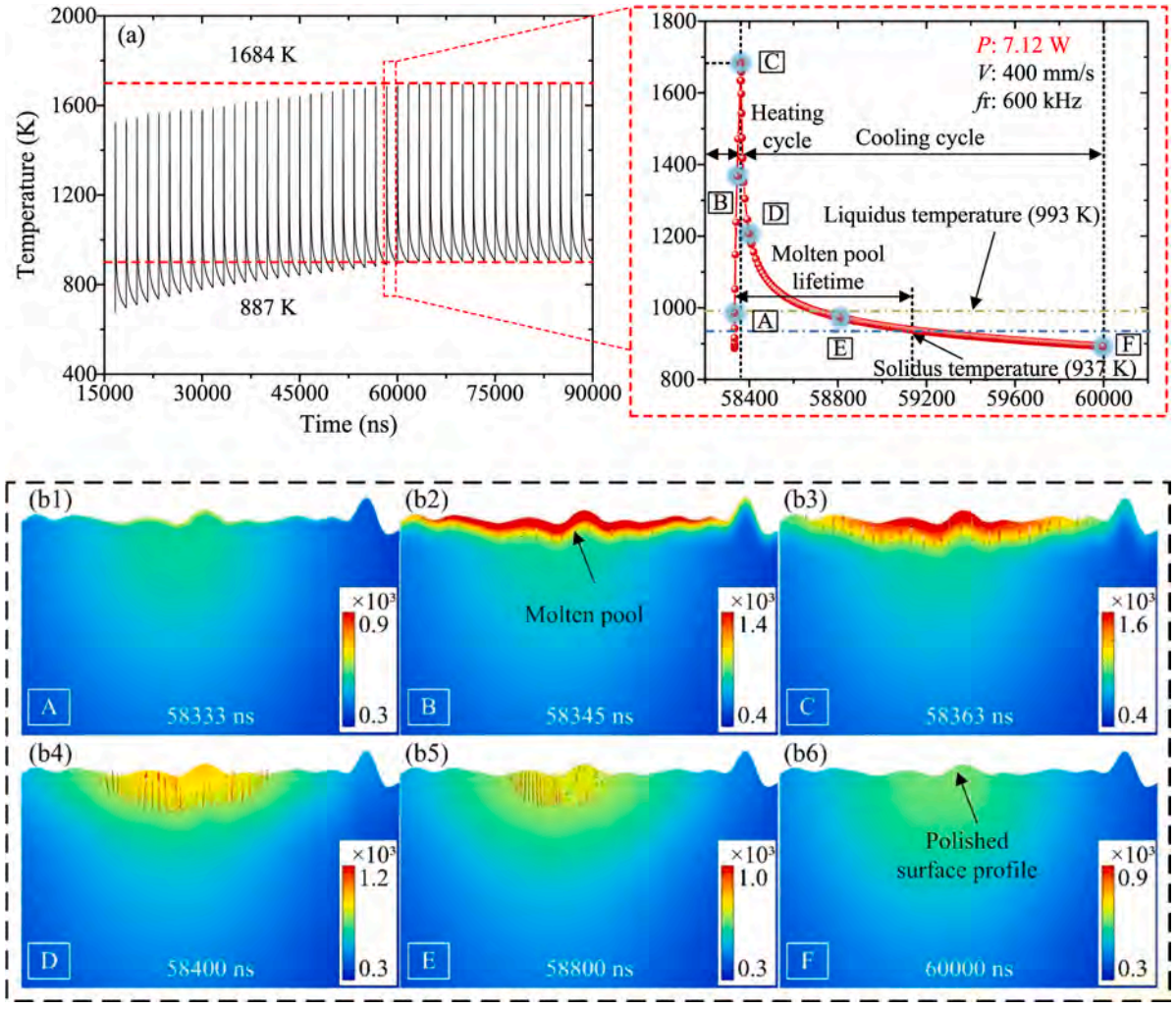

Fig. 12. The thermal cycle profiles and contours of molten pools obtained at different laser powers: (a)–(b) 7.12 W, (c)–(d) 10.5 W, and (e)–(f) 13.7 W.

indicated in Fig. 10(a), which may be an indicator for the insufficient melting of materials owing to a low heat input. To verify this speculation, the corresponding numerical simulation is performed, and the instantaneous change in the contours of molten pools at different laser powers is depicted Fig. 11. It is observed that after laser irradiation duration of 6696 ns, no significant change appears in the contours of molten pools (Fig. 11(a1), (b1), and (c1)). Upon applying the laser power of 13.7 W and a laser irradiation duration of 15030 ns, the surface roughness gradually decreases due to the cumulative effect of heat, exhibiting a tendency towards smoothing (Fig. 11(c2)). When the laser irradiation duration increases to 66697 ns and 70030 ns, the contours of molten pools at the laser power of 13.7 W remain relatively stable (Fig. 11(c4)–(c5)). In contrast, for the laser powers of 7.12 W and 10.5 W, the smoothing of the surface contour experiences a slight delay (Fig. 11(a2)–(a5) and Fig. 11(b2)–(b5)), and there are some differences in the stable contour shape. For revealing the hydrodynamic behavior of molten materials, a comprehensive analysis is conducted on the temperature and velocity distribution of a representative pulse period in the stabilization stage.

Fig. 12(a) presents the time-varying maximum temperature at the laser power of 7.12 W. It is evident that with an increase in the pulse number, the maximum temperature tends to increase due to heat accumulation and eventually stabilizes at 1684 K, indicating the attainment of a stabilization stage in the heat exchange process. Then, the contour evolution of molten pool within a pulse period, from 58333 ns to 60000 ns of laser irradiation duration, is shown in Fig. 12(b1)–(b6). It is observed that the temperature of LP region exceeds the liquidus temperature (993 K) at 58333 ns. This results in the generation of a molten pool, which is depicted at time point A in Fig. 12(b1). Under continuous laser irradiation, the temperature of LP region increases sharply until reaching a peak temperature (1684 K) at 58363 ns. At this time, the dimension of molten pool exhibits a significant increase compared to that at time point A, and the flow of the molten materials is governed by the combined influence of gravity and surface tension. Subsequently, the temperature of molten pool rapidly decreases and falls below the solidus temperature (937 K) within 59140 ns due to the laser beam being turned off. Corresponding to the temperature change from time point C to time point E, the dimension of molten pool decreases continuously as shown in Fig. 12(b3)–(b5). Upon analyzing the thermal cycle profile and instantaneous contour of molten pool obtained at the laser power of 7.12 W, it is apparent that only partial melted micro-peaks flow into the micro-valleys within a lifetime of 807 ns. Thus, some surface defects including undulations and particles still remain on the LP surface as illustrated at time point F in Fig. 12(b6).

When increasing laser power to 10.5 W, no evident surface defects are observed except for the laser-remelted tracks as presented in Fig. 10 (b). Given the thermal cycle profile illustrated in Fig. 12(c), this phenomenon should be because the temperature of LP region always remains between the liquidus temperature (993 K) and the vaporization temperature (3792 K). Accordingly, the lifetime of molten pool is

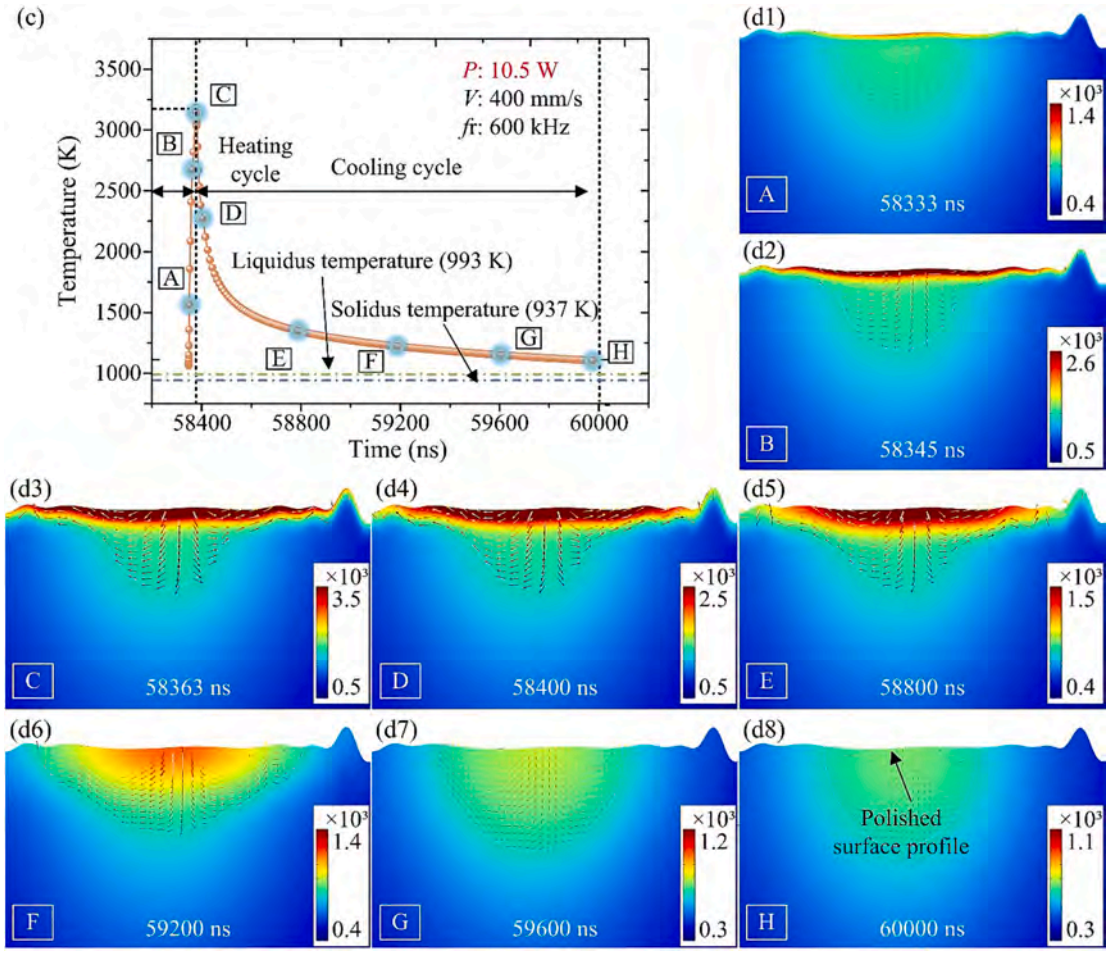

Fig. 12. (*continued*).

considerably prolonged to 1667 ns, and molten micro-peak materials sufficiently flow into the micro-valleys under the action of gravity and surface tension (see Fig. 12(d1)–(d8)). While at the laser power of 13.7 W, plenty of micro-cracks appear on the LP surface (see Fig. 10(c)). This is due to that temperature of molten pool significantly exceeds vaporization temperature (3792 K) during the laser irradiation duration from 58342 ns to 58365 ns, as indicated in Fig. 12(e). The resultant temperature gradient intensifies, inducing the development of thermal stress, ultimately causing the initiation and propagation of micro-cracks [63,64]. Additionally, the evident surface deformation is visible on the LP surface as displayed in Fig. 10(c). This is primarily due to that the recoil pressure resulting from vapors escaping from the evaporation surface dominates the fluid flow, and thus the molten materials dramatically flow to the bottom of molten pool (see Fig. 12(f2)–(f3)). Upon termination of the laser pulse after a duration of 30 ns, the temperature drops swiftly below the vaporization temperature (3792 K), causing the recoil pressure to cease action. Despite this, the downward flow of materials within the molten pool persists due to the collective influences of gravity and the preceding recoil pressure (see Fig. 12(f4)–(f6)). With this premise, the current surface quality deteriorates significantly compared to that obtained at the laser power of 10.5 W, which is consistent with the results of surface roughness in Fig. 8(j).

The surface morphologies changing with the scanning speed at the laser power of 10.5 W and pulse frequency of 600 kHz are illustrated in Fig. 10(d)–(f). To provide characterization of the thermal behavior during LP, the corresponding thermal cycle profiles are displayed. In Fig. 10(d), at the scanning speed of 200 mm/s, numerous micro-cracks can be observed throughout the LP surface; while at the scanning speed of 500 mm/s or 600 mm/s, surface undulations and un-melted particles are clearly observed, even accompanied by micron-sized surface defects. Interestingly, even though the LP surfaces exhibit the markedly distinct features, the corresponding thermal cycle profiles display hardly any noticeable difference (see Fig. 13). This should be because during LP, the scanning speed primarily impacts the spatial distribution of discrete laser pulses, thereby affecting the heat accumulation in the LP region (see Eq. (11)). Consequently, at the scanning speed of 200 mm/s, the spatial distance between adjacent laser pulses is relatively small, resulting in the excessive heat accumulation and thus the formation of microcracks. However, when the scanning speed reaches above 500 mm/s, the increased spatial distance causes the decrease of heat accumulation and limits the sufficient melting of materials, leading to several un-melted particles and surface defects.

Additionally, the morphologies of LP surfaces are further investigated by varying the pulse frequency while maintaining a constant laser power of 10.5 W and scanning speed of 400 mm/s. The resulting SEM morphologies and thermal cycle profiles are displayed in Fig. 10(g)–(i) and Fig. 14, respectively. It is seen that the peak temperature in the thermal cycle profile obtained at the pulse frequency of 400 kHz (4635 K) significantly exceeds the vaporization temperature (3792 K); while the peak temperature obtained at the pulse frequency of 800 kHz (3085 K) or 1000 kHz (2562 K) is always in the range between the liquidus temperature (993 K) and the vaporization temperature (3792 K). This implies at the pulse frequency of 400 kHz, more heat has been introduced to melt the surface materials and even start an ablation process. On the other hand, compared to the pulse frequency of 800 kHz or 1000 kHz, utilizing the pulse frequency of 400 kHz results in a larger spatial distance and time interval between the adjacent laser pulses, which would intensity the inhomogeneity of the temperature distribution.

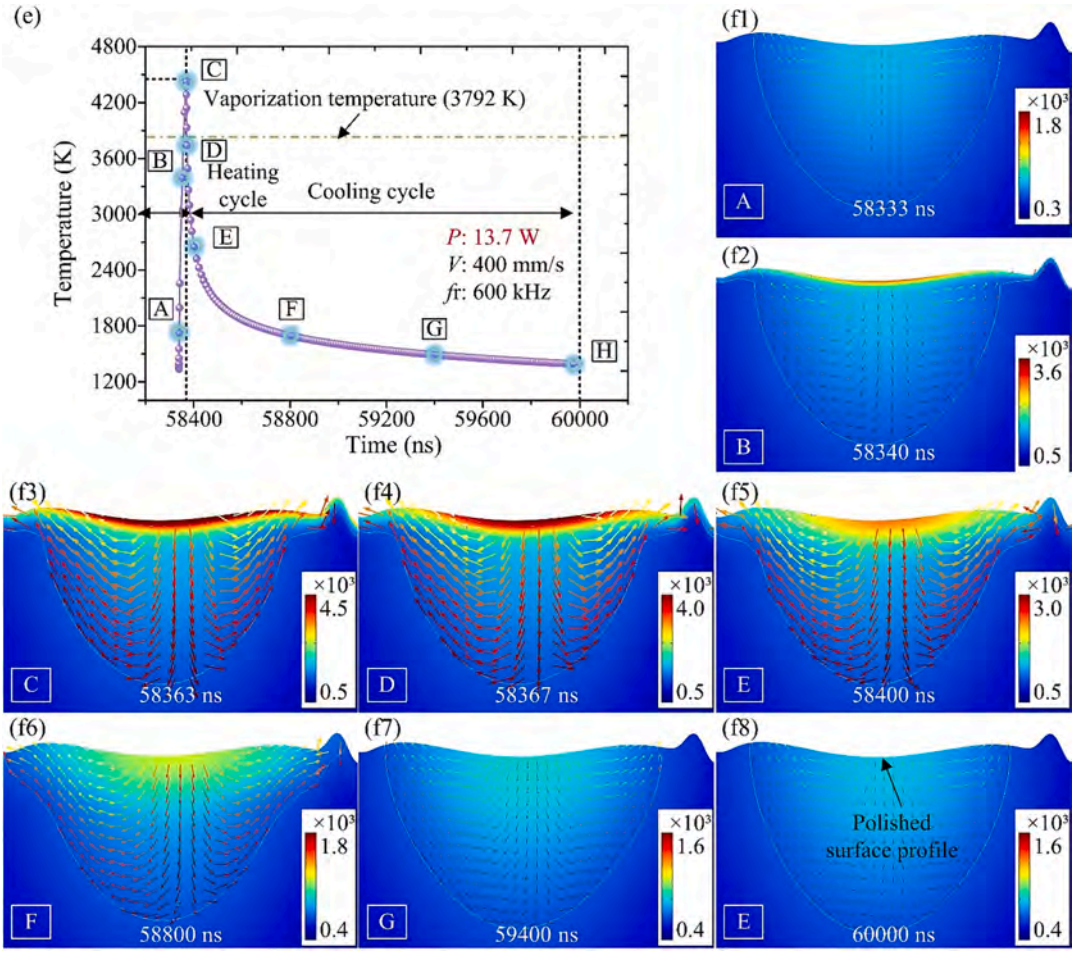

Fig. 12. (*continued*).

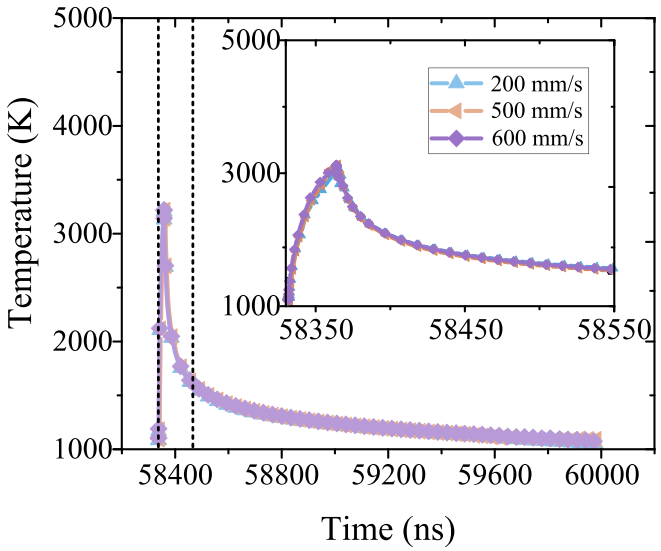

Fig. 13. The thermal cycle profiles of the LP regions obtained at different scanning speeds.

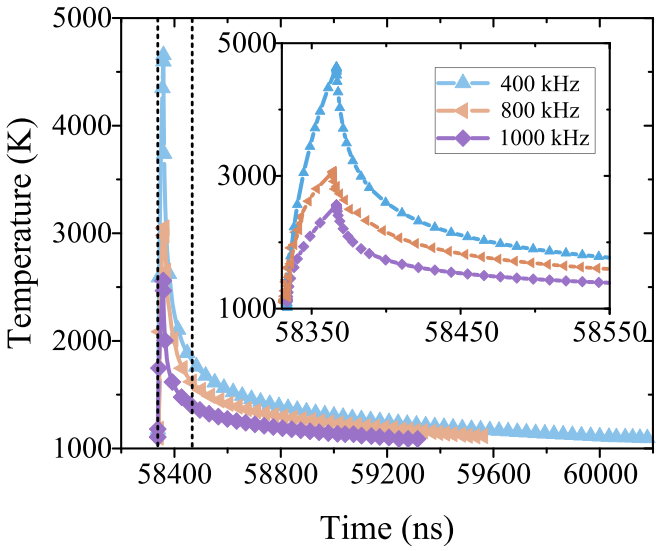

Fig. 14. The thermal cycle profiles of the LP regions obtained at the pulse frequencies of 400 kHz, 800 kHz, and 1000 kHz.

Overall, the collective influence of the aforementioned factors intensifies the temperature gradient between the high and low temperature regions when operating at the pulse frequency of 400 kHz, which triggers a considerable number of micro-cracks and asperities (Fig. 10(g)). In comparison, at the higher pulse frequencies of 800 kHz and 1000 kHz, the pulse distribution is more uniform, thus the relatively flat surfaces with only laser-remelted tracks and subtle surface undulations are visible as displayed in Fig. 10(h) and 10(i).

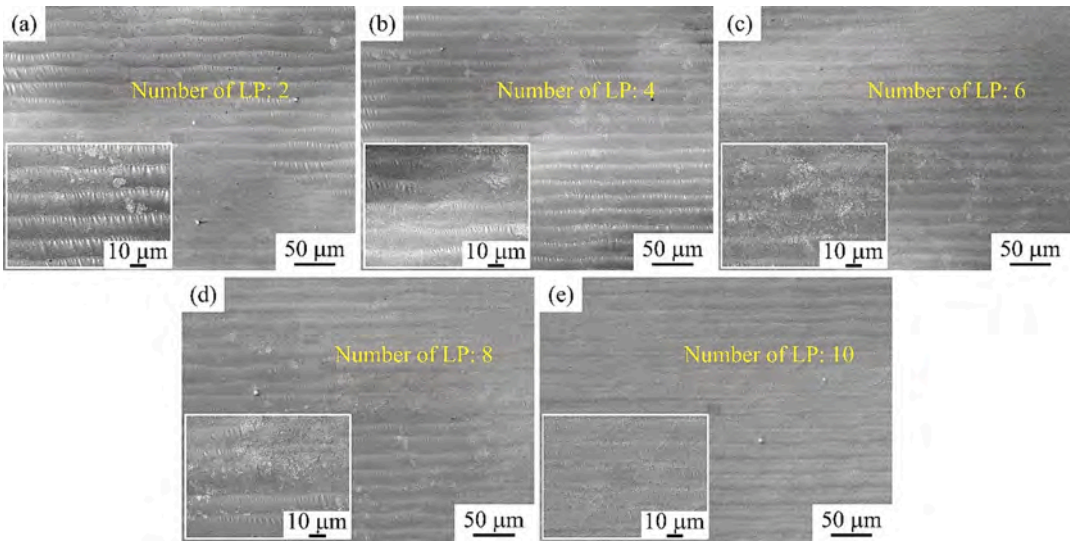

Fig. 15. SEM morphology of the WEDMS4 surface changing with the number of LP: (a) 2, (b) 4, (c) 6, (d) 8, and (e) 10.

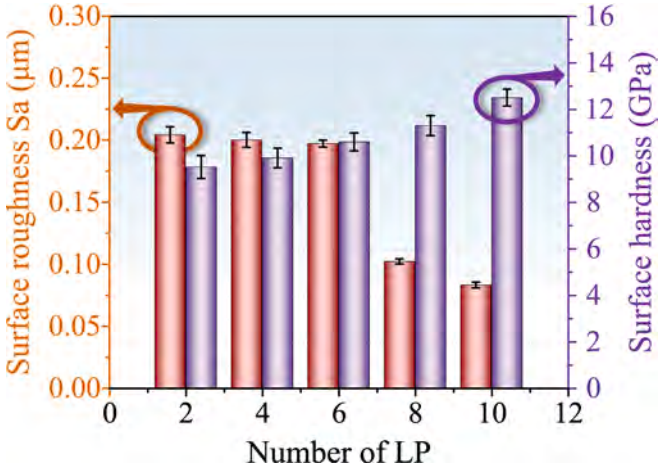

Fig. 16. Hardness and roughness of WEDMS4 surface changing with the number of LP.

4.3. Effect of the number of LP on surface quality

By evaluating the variations in roughness and morphology of the WEDMed MG surfaces under various LP parameters, the effectiveness of LP in improving surface quality can be clearly observed. Nevertheless, there are still some surface undulations on the LP surface after performing single LP, especially for the surfaces with higher initial roughness (WEDMS3 and WEDMS4 surfaces). This observation may be attributed to the collective influence of several factors. Firstly, the rapid remelting and cooling process of pulsed LP may result in the inadequate filling of the micro-peak materials into the distant micro-valleys. Moreover, the Gaussian distribution of the laser beam can potentially cause inhomogeneity of the laser energy deposited on the LP region. Therefore, it is considered to employ continuous multiple LP to reduce undulations by repetitively inducing surface melting. For brevity, the evolution of the surface morphology after multiple LP and corresponding surface roughness are detailed only for WEDMS4 surface, as displayed in Figs. 15 and 16. It is apparent that when the number of LP increases from 2 to 10, the spatial undulations are gradually weakened, and the surface roughness decreases continuously from 0.204 μm to 0.083 μm. After performing 10 remelting cycles, a uniform LP surface virtually free of surface defects is obtained in Fig. 15(e). On the other hand, an increment in the number of LP is expected to result in an extended duration of the melting process, possibly enhancing the reaction of nitrogen and zirconium elements. Thus, to further investigate the surface properties shown in Fig. 15(a)–(e), a comprehensive analysis is performed by combining EDS and nanoindentation tests, and the results are shown in Fig. 16 and Table 6. Evidently, both surface hardness and the content of nitrogen element exhibit a gradual rise with an increase in the number of LP. The above results indicate that executing repeated LP on the same region can effectively mitigate the spatial undulations by facilitating more frequent remelting of materials, and simultaneously improve the surface hardness as well.

Table 6
Element content for WEDMS4 surface treated by different numbers of LP.

Number of LP	Element content				
	Zr (at. %)	Ti (at. %)	Cu (at. %)	Ni (at. %)	N (at. %)
2	49.93	15	11.19	10.46	13.42
4	50.49	14.64	11.07	9.73	14.06
6	48.46	14.89	10.95	9.88	15.82
8	49.85	14.19	9.54	8.62	17.80
10	51.13	12.18	5.58	6.59	24.52

4.4. Mechanism of LP and simultaneous hardening

To reveal the mechanism of LP and simultaneous hardening, the cross-sections of the WEDMS4 surface and its surface after 10 times of LP are provided in Fig. 17. In Fig. 17(a) and (b), the WEDMS4 surface exhibits an observably rough cross-sectional profile, accompanied by some cracks and pores. However, after LP, the defects caused by WEDM disappear, and the cross-sectional profile becomes smoother, alongside the formation of an affecting layer (Fig. 17(c) and (d)). Within this affecting layer, large numbers of cluster-like structures are evenly distributed. Subsequently, EDS line scanning was performed along the depth direction of the cross-sections of the WEDMS4 surface and its LP surface to analyze the element distribution. The measurement origination is the top surfaces of the cross-sections. The EDS results indicate that four main elements (Zr, Ti, Cu, Ni) of the MG substrate are detected in the cross-section of the WEDMS4 surface, and the elemental content nearly does not change along the depth direction, as illustrated in Fig. 18 (a). While for the LP surface, N element could be detected, and the concentration of Zr and N elements within the affecting layer exceeds that of the MG substrate, as shown in Fig. 18(b) and (c). This observation is consistent with the XRD results presented in Fig. 7 and provides

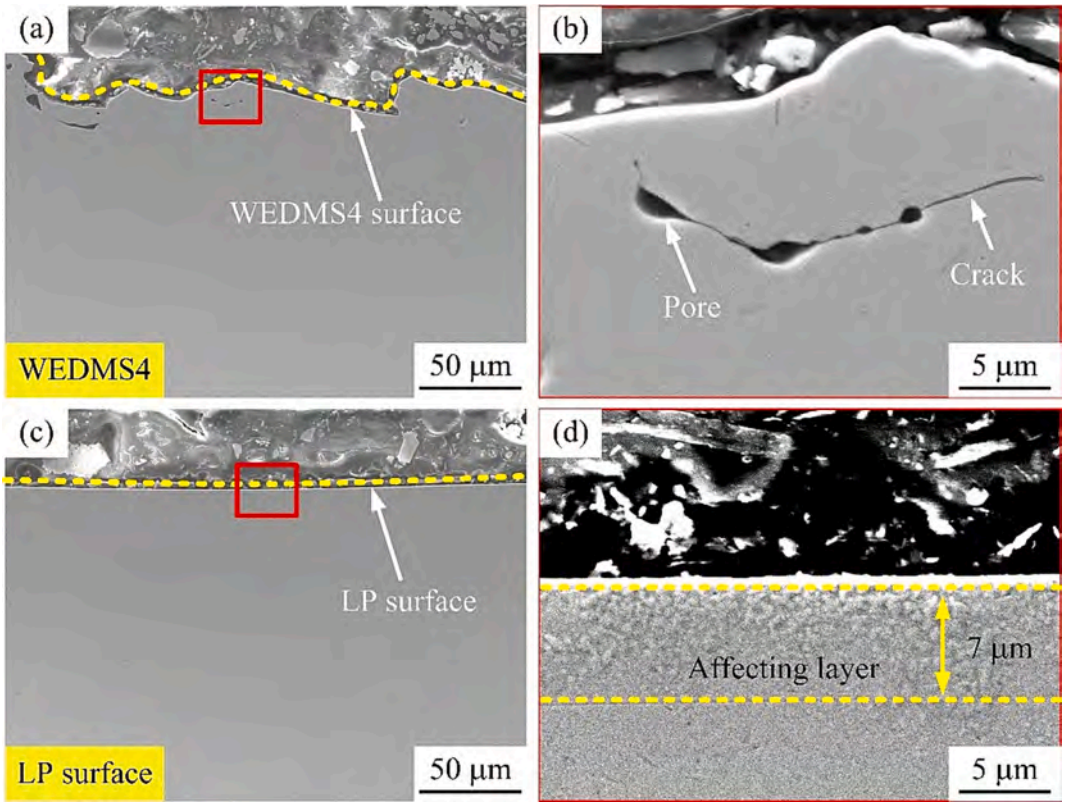

Fig. 17. (a) and (c) illustrate the SEM morphologies of the cross-sections of WEDMS4 surface and its LP surface. (b) and (d) are local enlarged images of Fig. 17(a) and (c), respectively.

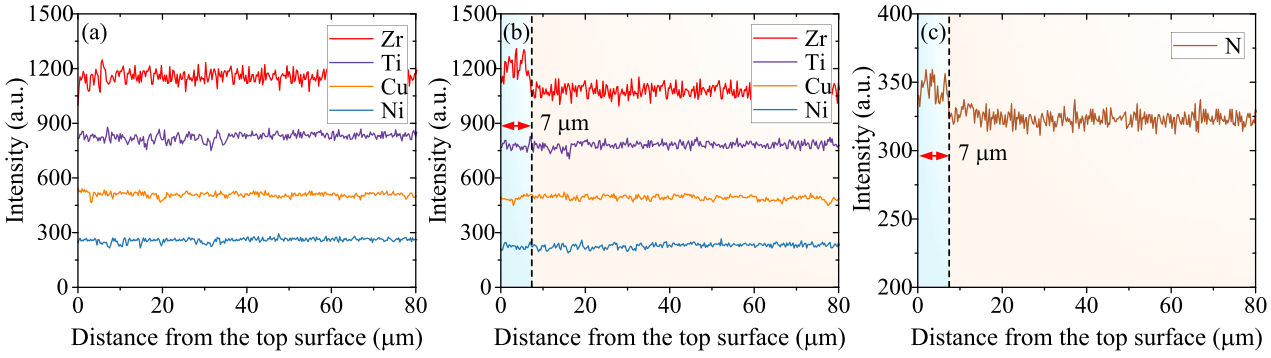

Fig. 18. Element distribution of (a) WEDMS4 surface and (b)-(c) its LP surface along the depth direction of the cross-sections.

additional evidence for the formation of the nitride phase.

Based on simulation and experimental analysis, a schematic diagram is illustrated in Fig. 19 to qualitatively describe the mechanism of LP and simultaneous hardening. With the action of the laser beam, the irradiated area undergoes heat transfer, leading to a temperature increase, as shown in Fig. 19(a). When the temperature in the irradiated area rises above the liquidus temperature of MG, a liquid molten pool is generated (Fig. 19(b)). Nitrogen molecules are absorbed at the air/molten pool interface through convection and diffusion, and subsequently dissociate into nitrogen atoms [65,66]. Due to the chemical affinity between zirconium atoms and nitrogen atoms at high temperature, the nitrogen atoms in the surface of the molten pool combine with zirconium atoms, forming ZrN phases (Fig. 19(b) and (c)). These in-situ generated ZrN phases continue to move within the molten pool with the role of Marangoni convection and tend to distribute uniformly in the MG substrate during multiple LP. Simultaneously, driven by surface tension, the liquid materials tend to redistribute, which means that the micro-peak materials of the WEDMed surface liquefy and flow towards the micro-valleys. When the laser beam proceeds, the ZrN phases begin to precipitate and grow from the liquid phase during rapid cooling. As a result, a smooth surface embedded with the ZrN phases is obtained, as shown in the Fig. 19(d).

5. Conclusion

This paper aimed to explore the feasibility of employing pulsed LP as an approach for simultaneously improving the surface quality and hardness of WEDMed Zr-based MG surfaces. The evolution of surface roughness, morphology and hardness under different LP parameters including the pulse width, pulse frequency, laser power, and scanning speed were systematically evaluated. Based on experimental and simulation analysis, several conclusions can be drawn:

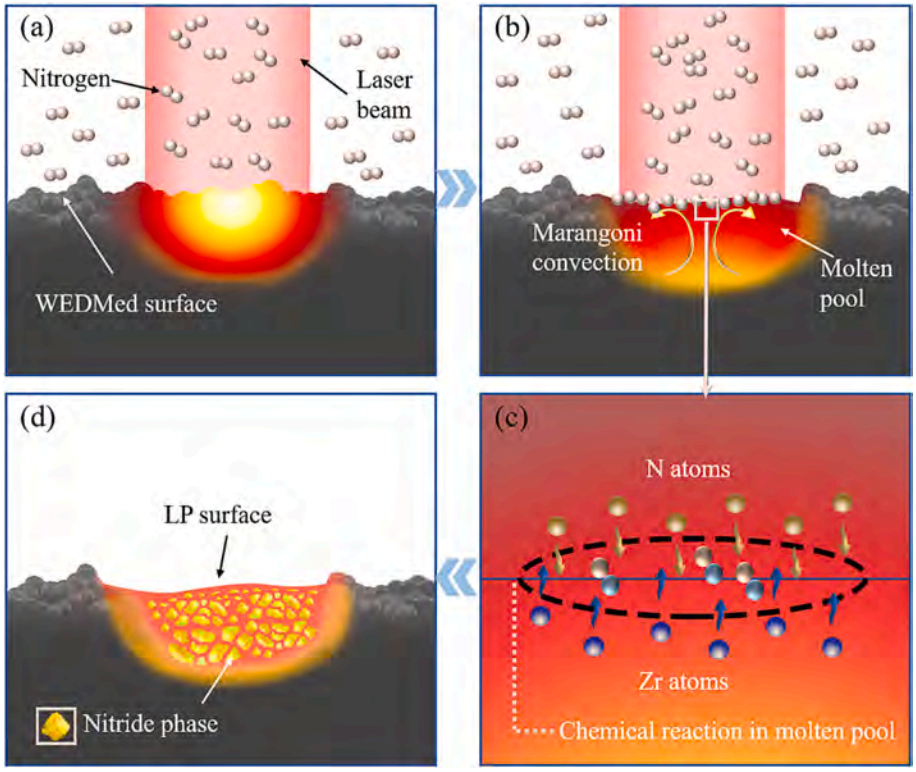

Fig. 19. Schematic diagram illustrating the mechanism of LP and simultaneous hardening. (a) Heat transfer in the irradiated area; (b) formation of a molten pool; (c) interaction between Zr atoms and N atoms; (d) formation of a smooth surface with ZrN phases embedded.

(1) The roughness (Sa) of the WEDMS1-WEDMS4 surfaces was remarkably reduced from 1.27, 2.10, 3.49, and 4.58 μm to 0.09, 0.14, 0.17, and 0.21 μm, respectively, after performing single LP on four representative WEDMed surfaces using the optimized laser parameters. Correspondingly, the microstructure evolution from the WEDMS1-WEDMS4 surfaces to the SLP1-SLP4 surfaces indicated an evident increase in the surface flatness as well.

(2) In comparison with the as-cast MG surface, the hardness of the SLP1-SLP4 surfaces exhibited a pronounced increase. According to the XRD results, the formation of ZrN phase during LP is responsible for this improvement in hardness.

(3) The pulse width, laser power, and pulse frequency were able to tailor the heat input acting on the surface materials; while the pulse frequency and scanning speed can determine the surface remelting times per unit area or per unit time. These laser parameters jointly influenced the temperature distribution and flow behavior of the molten pool, and determined the final effect of LP.

(4) Taking WEDMS4 surface as a representative example, as the number of LP increased from 2 to 10, the spatial undulations were gradually weakened, and the surface roughness decreased continuously from 0.204 μm to 0.083 μm, alongside a gradual increase in surface hardness. These results indicated that executing repeated LP on the same region can effectively mitigate the spatial undulations by facilitating more frequent remelting of materials, and simultaneously improve the surface hardness as well.

This study verifies the feasibility of employing pulsed LP as an approach for simultaneously improving the quality and hardness of WEDMed Zr-based MG surfaces. In the current study, the surface roughness, morphology evolution and mechanical properties have been systematically investigated. While, to further expand the application prospects of MGs, the friction performance could require further analysis and evaluation in the future.

CRediT authorship contribution statement

Jing Hong: Writing – original draft, Visualization, Validation, Software, Methodology, Investigation, Formal analysis, Data curation. **Hu Huang:** Writing – review & editing, Supervision, Resources, Project administration, Methodology, Investigation, Funding acquisition, Conceptualization. **Lin Zhang:** Investigation, Data curation. **Zhiyu Zhang:** Resources, Investigation. **Minqiang Jiang:** Resources, Investigation. **Jiwang Yan:** Supervision, Methodology.

Declaration of competing interest

The authors declare that they have no known competing financial interests or personal relationships that could have appeared to influence the work reported in this paper.

Data availability

Data will be made available on request.

Acknowledgements

This work was supported by the Natural Science Foundation of Jilin Province (20220101198JC), National Outstanding Youth Science Fund Project (No. 12125206) of NSFC, and the Fundamental Research Funds for the Central Universities (2020-2023).

References

[1] M.W. Chen, A brief overview of bulk metallic glasses, Npg Asia Mater. 3 (2011) 82–90, https://doi.org/10.1038/asiamat.2011.30.
[2] M.M. Trexler, N.N. Thadhani, Mechanical properties of bulk metallic glasses, Prog. Mater. Sci. 55 (2010) 759–839, https://doi.org/10.1016/j.pmatsci.2010.04.002.
[3] J.R. Scully, A. Gebert, J.H. Payer, Corrosion and related mechanical properties of bulk metallic glasses, J. Mater. Res 22 (2006) 302–313, https://doi.org/10.1557/jmr.2007.0051.

[4] C.A. Schuh, T.C. Hufnagel, U. Ramamurty, Mechanical behavior of amorphous alloys, Acta Mater. 55 (2007) 4067–4109, https://doi.org/10.1016/j.actamat.2007.01.052.

[5] A. Inoue, X.M. Wang, W. Zhang, Developments and applications of bulk metallic glasses, Rev. Adv. Mater. Sci. 18 (2008) 1–9.

[6] K. Weinert, D. Biermann, S. Bergmann, Machining of high strength light weight alloys for engine applications, CIRP Annals 56 (2007) 105–108, https://doi.org/10.1016/j.cirp.2007.05.027.

[7] M. Bakkal, A.J. Shih, S.B. Mcspadden, R.O. Scattergood, Thrust force, torque, and tool wear in drilling the bulk metallic glass, Int. J. Mach. Tools Manu. 45 (2005) 863–872, https://doi.org/10.1016/j.ijmachtools.2004.11.005.

[8] X. Chen, J.F. Xiao, Y. Zhu, R.J. Tian, X.W. Shu, J.F. Xu, Micro-machinability of bulk metallic glass in ultra-precision cutting, Mater. Des. 136 (2017) 1–12, https://doi.org/10.1016/j.matdes.2017.09.049.

[9] T. Wang, X.Y. Wu, G.Q. Zhang, B. Xu, Y.H. Chen, S.C. Ruan, Experimental Study on Machinability of Zr-Based Bulk Metallic Glass during Micro Milling, Micromachines 11 (2020) 86, https://doi.org/10.3390/mi11010086.

[10] N.K. Maroju, D.P. Yan, B.Y. Xie, X.L. Jin, Investigations on surface microstructure in high-speed milling of Zr-based bulk metallic glass, J. Manuf. Process. 35 (2018) 40–50, https://doi.org/10.1016/j.jmapro.2018.07.020.

[11] M. Bakkal, C.T. Liu, T.R. Watkins, R.O. Scattergood, A.J. Shih, Oxidation and crystallization of Zr-based bulk metallic glass due to machining, Intermetallics 12 (2004) 195–204, https://doi.org/10.1016/j.intermet.2003.09.017.

[12] J. Xiong, H. Wang, G.Q. Zhang, Y.B. Chen, J. Ma, R.D. Mo, Machinability and Surface Generation of Pd40Ni10Cu30P20 Bulk Metallic Glass in Single-Point Diamond Turning, Micromachines 11 (2020) 4, https://doi.org/10.3390/mi11010004.

[13] C.G. Tang, Y. Li, K.Y. Zeng, Characterization of mechanical properties of a Zr-based metallic glass by indentation techniques, Mater. Sci. Eng. A 384 (2004) 215–223, https://doi.org/10.1016/j.msea.2004.06.013.

[14] N.K. Maroju, X.L. Jin, Mechanism of chip segmentation in orthogonal cutting of Zr-based bulk metallic glass, J Manuf Sci E-T ASME 141 (2019), 081003, https://doi.org/10.1115/1.4043837.

[15] M. Bakkal, A.J. Shih, R.O. Scattergood, Chip formation, cutting forces, and tool wear in turning of Zr-based bulk metallic glass, Int. J. Mach. Tools Manu. 44 (2004) 915–925, https://doi.org/10.1016/j.ijmachtools.2004.02.002.

[16] S. Chakraborty, V. Dey, S.K. Ghosh, A review on the use of dielectric fluids and their effects in electrical discharge machining characteristics, Precis. Eng. 40 (2014) 1–6, https://doi.org/10.1016/j.precisioneng.2014.11.03.

[17] H. Takino, T. Ichinohe, K. Tanimoto, S. Yamaguchi, K. Nomura, M. Kunieda, Cutting of polished single-crystal silicon by wire electrical discharge machining, Precis. Eng. 28 (2004) 314–319, https://doi.org/10.1016/j.precisioneng.2003.12.002.

[18] S.F. Hsieh, S.L. Chen, M.H. Lin, S.F. Ou, W.T. Lin, M.S. Huang, Crystallization and carbonization of an electrical discharge machined Zr-based bulk metallic glass alloy, J. Mater. Res. 28 (2013) 3177–3184, https://doi.org/10.1557/jmr.2013.329.

[19] R. Chaudhari, J.J. Vora, S.S. Mani Prabu, I.A. Palani, V.K. Patel, D.M. Parikh, L.n. l. De Lacalle, Multi-response optimization of WEDM process parameters for machining of superelastic nitinol shape-memory alloy using a heat-transfer search algorithm, Materials 12 (2019) 1277, https://doi.org/10.3390/ma12081277.

[20] R. Chaudhari, J.J. Vora, S.S. Mani Prabu, I.A. Palani, V.K. Patel, D.M. Parikh, Pareto optimization of WEDM process parameters for machining a NiTi shape memory alloy using a combined approach of RSM and heat transfer search algorithm, Adv. Manuf. 9 (2021) 64–80, https://doi.org/10.1007/s40436-019-00267-0.

[21] R. Chaudhari, I. Ayesta, M. Doshi, S. Khanna, V.K. Patel, J. Vora, L.N.L. De Lacalle, Effect of Multi-walled carbon nanotubes on the performance evaluation of Nickel-based super-alloy–Udimet 720 machined using WEDM process, Int. J. Adv. Manuf. Tech. 123 (2022) 2087–2105, https://doi.org/10.1007/s00170-022-10209-z.

[22] Z. Chen, C. Wu, H.B. Zhou, G.J. Zhang, H.Z. Yan, A high-efficiency preparation method of super wear-resistant superhydrophobic surface with hierarchical structure using wire electrical discharge machining, Surf. Coat. Technol. 444 (2022), 128673, https://doi.org/10.1016/j.surfcoat.2022.128673.

[23] H. Huang, J.W. Yan, Microstructural changes of Zr-based metallic glass during microelectrical discharge machining and grinding by a sintered diamond tool, J. Alloy Compd. 688 (2016) 14–21, https://doi.org/10.1016/j.jallcom.2016.07.181.

[24] X.Y. Wu, S.J. Li, Z. Jia, B. Xin, X.C. Yin, Using WECM to remove the recast layer and reduce the surface roughness of WEDM surface, J. Mater. Process. Tech. 268 (2019) 140–148, https://doi.org/10.1016/j.jmatprotec.2019.01.016.

[25] M.C. Reddy, K.V. Rao, G. Suresh, An experimental investigation and optimization of energy consumption and surface defects in wire cut electric discharge machining, J. Alloy Compd. 861 (2021), 158582, https://doi.org/10.1016/j.jallcom.2020.158582.

[26] Z.Q. Zeng, Y.K. Wang, Z.L. Wang, D.B. Shan, X.L. He, A study of micro-EDM and micro-ECM combined milling for 3D metallic micro-structures, Precis. Eng. 36 (2012) 500–509, https://doi.org/10.1016/j.precisioneng.2012.01.005.

[27] N. Ma, X.L. Yang, M.Q. Gao, J.L. Song, G.L. Liu, W.J. Xu, A study of electrodischarge machining–pulse electrochemical machining combined machining for holes with high surface quality on superalloy, Adv. Mech. Eng. 7 (2015), 1687814015618630, https://doi.org/10.1177/1687814015618630.

[28] B.H. Yan, G.W. Chang, J.H. Chang, R.T. Hsu, Improving electrical discharge machined surfaces using magnetic abrasive finishing, Mach. Sci. Technol. 8 (2004) 103–118, https://doi.org/10.1081/MST-120034246.

[29] S.K. Amineh, A.F. Tehrani, A. Mohammadi, Improving the surface quality in wire electrical discharge machined specimens by removing the recast layer using magnetic abrasive finishing method, Int. J. Adv. Manuf. Technol. 66 (2013) 1793–1803, https://doi.org/10.1007/s00170-012-4459-7.

[30] D. Rakwal, S. Heamawatanachai, P. Tathireddy, F. Solzbacher, E. Bamberg, Fabrication of compliant high aspect ratio silicon microelectrode arrays using micro-wire electrical discharge machining, Microsyst. Technol. 15 (2009) 789–797, https://doi.org/10.1007/s00542-009-0792-7.

[31] T.T. Deng, J.J. Li, Z.Z. Zheng, Fundamental aspects and recent developments of metal surface polishing with energy beam irradiation, Int. J. Mach. Tools Manu. 148 (2020), 103472, https://doi.org/10.1016/j.ijmachtools.2019.103472.

[32] C.D. Giorgi, V. Furlan, A.G. Demir, E. Tallarita, G. Candiani, B. Previtali, Laser micropolishing of AISI 304 stainless steel surfaces for cleanability and bacteria removal capability, Appl. Surf. Sci. 406 (2017) 199–211, https://doi.org/10.1016/j.apsusc.2017.02.083.

[33] Z.F. Xu, W.T. Ouyang, Y.F. Liu, J.K. Jiao, Y.Z. Liu, W.W. Zhang, Effects of laser polishing on surface morphology and mechanical properties of additive manufactured TiAl components, J. Manuf. Process. 65 (2021) 51–59, https://doi.org/10.1016/j.jmapro.2021.03.014.

[34] A. Temmler, D. Liu, J. Preußner, S. Oeser, J. Luo, R. Poprawe, J.H. Schleifenbaum, Influence of laser polishing on surface roughness and microstructural properties of the remelted surface boundary layer of tool steel H11, Mater. Des. 192 (2020), 108689, https://doi.org/10.1016/j.matdes.2020.108689.

[35] H. Huang, J. Hong, Y.F. Qian, C. Wang, Z.Y. Zhang, L. Zhang, Nanosecond laser polishing of laser nitrided Zr-based metallic glass surface, Int. J. Adv. Manuf. Tech. 121 (2022) 4099–4113, https://doi.org/10.1007/s00170-022-09606-1.

[36] A. Sassmannshausen, A. Brenner, J. Finger, Ultrashort pulse laser polishing by continuous surface melting, J. Mater. Process. Tech. 293 (2021), 117058, https://doi.org/10.1016/j.jmatprotec.2021.117058.

[37] Y.K. Xu, H. Ma, J. Xu, E. Ma, Mg-based bulk metallic glass composites with plasticity and gigapascal strength, Acta Mater. 53 (2005) 1857–1866, https://doi.org/10.1016/j.actamat.2004.12.036.

[38] Y.M. Zou, Z.G. Qiu, Z.G. Zheng, G. Wang, X.C. Yan, S. Yin, M. Liu, D.C. Zeng, Ex-situ additively manufactured FeCrMoCB/Cu bulk metallic glass composite with well wear resistance, Tribo. Int. 162 (2021), 107112, https://doi.org/10.1016/j.triboint.2021.107112.

[39] A.K. Singh, S.H. Alavi, S.R. Paital, N.B. Dahotre, S.P. Harimkar, Structural Relaxation and Nanocrystallization-Induced Laser Surface Hardening of Fe-Based Bulk Amorphous Alloys, JOM 66 (2014) 1080–1087, https://doi.org/10.1007/s11837-014-0974-3.

[40] J. Fornell, E. Pellicer, E. Garcia-Lecina, D. Nieto, S. Surinach, M.D. Baró, J. Sort, Structural and mechanical modifications induced on Cu47. 5Zr47. 5Al5 metallic glass by surface laser treatments, Appl. Surf. Sci. 290 (2014) 188–193, https://doi.org/10.1016/j.apsusc.2013.11.032.

[41] H. Huang, M.Q. Jiang, J.W. Yan, The coupling effects of laser thermal shock and surface nitridation on mechanical properties of Zr-based metallic glass, J. Alloy Compd. 770 (2019) 864–874, https://doi.org/10.1016/j.jallcom.2018.08.195.

[42] J. Hong, Y.F. Qian, L. Zhang, H. Huang, M.Q. Jiang, J.W. Yan, Laser nitriding of Zr-based metallic glass: An investigation by orthogonal experiments, Surf. Coat. Technol. 424 (2021), 127657, https://doi.org/10.1016/j.surfcoat.2021.127657.

[43] F.C. Li, M. Song, S. Ni, S.F. Guo, X.Z. Liao, Correlation between hardness and shear banding of metallic glasses under nanoindentation, Mater. Sci. Eng. A 657 (2016) 38–42, https://doi.org/10.1016/j.msea.2016.01.048.

[44] Y.H. Zhu, J. Fu, C. Zheng, Z. Ji, Structural and mechanica lmodifications induced on Zr-based bulk metallic glass by laser shock peening, Opt. Laser Technol. 86 (2016) 54–60, https://doi.org/10.1016/j.optlastec.2016.07.003.

[45] R. Busch, The thermophysical properties of bulk metallic glass-forming liquids, JOM 52 (2000) 39–42, https://doi.org/10.1007/s11837-000-0160-7.

[46] A. Peker, W.L. Johnson, A highly processable metallic glass: Zr41. 2Ti13. 8Cu12. 5Ni10. 0Be22. 5, Appl. Phys. Lett. 63 (1993) 2342-2344. https://doi.org/10.1063/1.110520.

[47] B. Singh, J.P. Misra, Surface finish analysis of wire electric discharge machined specimens by RSM and ANN modeling, Measurement 137 (2019) 225–237, https://doi.org/10.1016/j.measurement.2019.01.044.

[48] E.V. Bordatchev, A.M.K. Hafiz, O.R. Tutunea-Fatan, Performance of laser polishing in finishing of metallic surfaces, Int. J. Adv. Manuf. Technol. 73 (2014) 35–52, https://doi.org/10.1007/s00170-014-5761-3.

[49] L. Chen, B. Richter, X.Z. Zhang, K.B. Bertsch, D.J. Thoma, F.E. Pfefferkorn, Effect of laser polishing on the microstructure and mechanical properties of stainless steel 316L fabricated by laser powder bed fusion, Mater. Sci. Eng. A 802 (2021), 140579, https://doi.org/10.1016/j.msea.2020.140579.

[50] R.A. Conner, A.J. Rosakis, W.L. Johnson, D.M. Owen, Fracture toughness determination for a beryllium-bearing bulk metallic glass, Scripta Mater. 37 (1997) 1373–1378, https://doi.org/10.1016/s1359-6462(97)00250-9.

[51] C.G. Fan, H.H. Liao, H. Choo, P.K. Liaw, N. Mara, A.V. Sergueeva, A.K. Mukherjee, E.J. Lavernia, Fracture of a Commercial Zr 41.2 Ti 13.8 Cu 12.5 Ni 10.0 Be 22.5 Bulk-Metallic Glass, Phys. Metall. Mater. Sci. 38 (2007) 2001–2005, https://doi.org/10.1007/s11661-007-9199-1.

[52] M.D. Demetriou, W.L. Johnson, Modeling the transient flow of undercooled glass-forming liquids, J. Appl. Phys. 95 (2004) 2857–2865, https://doi.org/10.1063/1.1645669.

[53] M.Q. Jiang, Y.P. Wei, G. Wilde, L.H. Dai, Explosive boiling of a metallic glass superheated by nanosecond pulse laser ablation, Appl. Phys. Lett. 106 (2015), 021904, https://doi.org/10.1063/1.4905928.

[54] P. Sharma, D. Chakradhar, S. Narendranath, Evaluation of WEDM performance characteristics of Inconel 706 for turbine disk application, Mater. Des. 88 (2015) 558–566, https://doi.org/10.1016/j.matdes.2015.09.036.
[55] A. Temmler, D. Liu, J. Luo, R. Poprawe, Influence of pulse duration and pulse frequency on micro-roughness for laser micro polishing (LμP) of stainless steel AISI 410, Appl. Surf. Sci. 510 (2020), 145272, https://doi.org/10.1016/j.apsusc.2020.145272.
[56] Y. Chao, Y. Liu, Z. Xu, W. Xie, L. Zhang, W. Ouyang, H. Wu, Z. Pan, J. Jiao, S. Li, G. Zhang, W. Zhang, L. Sheng, Improving superficial microstructure and properties of the laser-processed ultrathin kerf in Ti-6Al-4V alloy by water-jet guiding, J. Mater. Sci. Technol. 156 (2023) 32–53, https://doi.org/10.1016/j.jmst.2022.11.058.
[57] T. Ermergen, F. Taylan, Review on surface quality improvement of additively manufactured metals by laser polishing, Arab. J. Sci. Eng. 46 (2021) 7125–7141, https://doi.org/10.1007/s13369-021-05658-9.
[58] M.T.C. Chow, E.V. Bordatchev, G.K. Knopf, Experimental study on the effect of varying focal offset distance on laser micropolished surfaces, Int. J. Adv. Manuf. Tech. 67 (2013) 2607–2617, https://doi.org/10.1007/s00170-012-4677-z.
[59] Q.B. Meng, X.L. Zhou, J.H. Li, Z.Q. Cui, Y.D. Wang, H.L. Zhang, Z. Li, C.L. Qiu, High-throughput laser fabrication of Ti-6Al-4V alloy: Part I. Numerical investigation of dynamic behavior in molten Pool, J. Mater. Process. Tech. 59 (2020) 509–522, https://doi.org/10.1016/j.jmapro.2020.10.008.
[60] D. Bhaduri, P. Penchev, A. Batal, S. Dimov, S.L. Soo, S. Sten, U. Harrysson, Z. X. Zhang, H.S. Dong, Laser polishing of 3D printed mesoscale components, Appl. Surf. Sci. 405 (2017) 29–46, https://doi.org/10.1016/j.apsusc.2017.01.211.
[61] S.M. Basha, M. Bhuyan, M.M. Basha, N. Venkaiah, M.R. Sankar, Laser polishing of 3D printed metallic components: a review on surface integrity, Materials Today: Proceedings 26 (2020) 2047–2054, https://doi.org/10.1016/j.matpr.2020.02.443.
[62] A. Krishnan, F.Z. Fang, Review on mechanism and process of surface polishing using lasers, Front. Mech. Eng-Prc 14 (2019) 299–319, https://doi.org/10.1007/s11465-019-0535-0.
[63] X.M. Zhang, L.F. Ji, L.T. Zhang, W.H. Wang, T.Y. Yan, Polishing of alumina ceramic to submicrometer surface roughness by picosecond laser, Surf. Coat. Technol. 397 (2020), 125962, https://doi.org/10.1016/j.surfcoat.2020.125962.
[64] A. Choudhary, A. Sadhu, S. Sarkar, A.K. Nath, G. Muvvala, Laser surface polishing of NiCrSiBC–60WC ceramic-metal matrix composite deposited by laser directed energy deposition process, Surf. Coat. Technol. 404 (2020), 126480, https://doi.org/10.1016/j.surfcoat.2020.126480.
[65] S.K. Wu, K. Zheng, J.L. Zou, F. Jiang, X.H. Han, A study of the behavior and effects of nitrogen take-up from protective gas shielding in laser welding of stainless steel, J. Manuf. Process. 34 (2018) 477–485, https://doi.org/10.1016/j.jmapro.2018.06.031.
[66] Z.H. Feng, X.Y. Sun, P.B. Han, H. Fu, H.C. Dong, S. Guo, R. Su, J.H. Li, Microstructure and microhardness of a novel TiZrAlV alloy by laser gas nitriding at different laser powers, Rare Metals 39 (2020) 270–278, https://doi.org/10.1007/s12598-019-01362-8.
[67] K. Li, H.M. Zhou, Z.Y. Zhao, H. Zhou, J. Yin, J.C. Jin, A study on transient molten pool dynamics in laser polishing of Ti6Al4V using numerical simulation, J. Manuf. Process. 65 (2021) 478–490, https://doi.org/10.1016/j.jmapro.2021.03.045.